Monthly Notices
of the
ROYAL ASTRONOMICAL SOCIETY

MNRAS **480,** 1247–1262 (2018)
Advance Access publication 2018 July 18

doi:10.1093/mnras/sty1890

A physical model of the broad-band continuum of AGN and its implications for the UV/X relation and optical variability

Aya Kubota[1,2]★ and Chris Done[1]

[1]*Department of Physics, University of Durham, South Road, Durham DH1 3LE, UK*
[2]*Department of Electronic Information Systems, Shibaura Institute of Technology, 307 Fukasaku, Minuma-ku, Saitama-shi, Saitama 337-8570, Japan*

Accepted 2018 July 11. Received 2018 July 11; in original form 2018 March 29

ABSTRACT

We develop a new spectral model for the broad-band spectral energy distribution (SED) of active galactic nuclei (AGN). This includes an outer standard disc, an inner warm Comptonizing region to produce the soft X-ray excess and a hot corona. We tie these together energetically by assuming Novikov–Thorne emissivity, and use this to define a size scale for the hard X-ray corona as equal to the radius where the remaining accretion energy down to the black hole can power the observed X-ray emission. We test this on three AGN with well-defined SEDs as well as on larger samples to show that the average hard X-ray luminosity is always approximately a few per cent of the Eddington luminosity across a large range of Eddington ratio. As a consequence, the radial size scale required for gravity to power the X-ray corona has to decrease with increasing Eddington fraction. For the first time, we hardwire this into the spectral models, and set the hard X-ray spectral index self-consistently from the ratio of the hard X-ray luminosity to intercepted seed photon luminosity from the disc. This matches the observed correlation of steeper spectral index with increasing Eddington ratio, as well as reproducing the observed tight UV/X relation of quasars. We also include the reprocessed emission produced by the hot inner flow illuminating the warm Comptonization and standard disc regions and show that this predicts a decreasing amount of optical variability with increasing Eddington ratio as observed, though additional processes may also be required to explain the observed optical variability.

Key words: accretion, accretion discs – black hole physics – galaxies: Seyfert.

1 INTRODUCTION

Active galactic nuclei (AGN) are powered by mass accreting on to a supermassive black hole (SMBH). The well-known Shakura & Sunyaev (1973) disc model makes very simple predictions for this emission if it is emitted locally and thermalizes to a blackbody. The disc temperature increases inwards (modulo a stress-free inner boundary condition at the innermost stable circular orbit, $R_{\rm ISCO}$), so the total spectrum is the sum over all radii of these different temperature components (multicolour disc blackbody; e.g. Mitsuda et al. 1984). However, the observed spectral energy distribution (SED) of AGN is much more complex than this predicts. There is a ubiquitous tail at X-ray energies, as well as an unexpected upturn below 1 keV, termed the 'soft X-ray excess'.

The hard X-ray tail indicates that some part of the accretion energy is not dissipated in the optically thick disc (where it would thermalize) but is instead released in an optically thin region (e.g. Elvis et al. 1994). The resulting Comptonized spectrum from 1 to 100 keV indicates that this region has electron temperature $kT_{\rm e} \sim$ 40–100 keV and optical depth $\tau \sim$ 1–2 (Fabian et al. 2015; Lubiński et al. 2016).

The origin of the 'soft X-ray excess' is not well understood. It can be fitted by a second Comptonization region with very different parameters from the coronal emission, one where the electrons are warm, $kT_{\rm e} \sim$ 0.1–1 keV and optically thick $\tau \sim$ 10–25 (e.g. Magdziarz et al. 1998; Czerny et al. 2003; Gierliński & Done 2004b; Porquet et al. 2004; Petrucci et al. 2013; Middei et al. 2018). Alternatively, it could be produced by reprocessing/reflection of the coronal emission on the very inner disc, where extremely strong relativistic effects smear out the expected strong line emission from ionized material (Crummy et al. 2006). The fastest soft X-ray variability is correlated with, and lags behind, the hard X-ray variability, so some fraction of the soft X-ray excess must be produced from reprocessing/reflection of the corona flux (e.g. De Marco et al. 2013; Fabian et al. 2013). However, recent results have shown that the majority of the soft excess does not arise from reflection (Mehdipour et al. 2011, 2015; Noda et al. 2013; Matt et al. 2014; Boissay, Ricci

★ E-mail: aya@shibaura-it.ac.jp

& Paltani 2016; Porquet et al. 2018), favouring the warm Comptonization model.

The warm Comptonization scenario also helps to explain another puzzling component of the broad-band AGN SED, namely a ubiquitous downturn seen in the UV, at energies far below those expected for the peak disc temperature (e.g. Zheng et al. 1997; Davis, Woo & Blaes 2007). A warm Comptonization spectrum can extend across the absorption gap, connecting the UV downturn and the soft X-ray upturn with a single component (Elvis et al. 1994; Laor et al. 1997; Richards et al. 2006). This carries a dominant fraction of the luminosity in the SED of AGN at lower Eddington ratio, $L_{\rm bol}/L_{\rm Edd}$ (Jin et al. 2012a; Jin, Ward & Done 2012b), again arguing against a purely reprocessing/reflection origin for the soft X-ray excess, though some contribution could be present (e.g. Lawrence 2012). The SED of high $L_{\rm bol}/L_{\rm Edd}$ is instead dominated by disc emission, which can extend into the soft X-ray bandpass for the lowest mass, Narrow Line Seyfert-1 (NLS1) galaxies, but these still have a small fraction of their bolometric power emitted in a soft X-ray excess component (Jin et al. 2012a,b, 2013; Done et al. 2012, hereafter D12; Matzeu et al. 2017).

Neither of the Comptonization components is well understood. However, the warm Comptonization region is especially problematic as, unlike the hot corona, it does not have a clear counterpart in the much lower mass black hole binary systems (BHB). These often show spectra at $L_{\rm bol}/L_{\rm Edd} \sim 0.1$–$0.2$ that are dominated by the thermal accretion disc emission, with only a small tail to higher energies from a hot Comptonizating corona (e.g. Kubota, Makishima & Ebisawa 2001; Gierliński & Done 2004a; Steiner et al. 2009).

One obvious break in scaling between BHB and AGN is that the SMBHs have discs that peak in the UV rather than X-ray temperature range. The UV is a region in which atomic physics is extremely important whereas plasma physics dominates in BHB. None the less, the best models of the accretion disc structure including UV opacities (Hubeny et al. 2001) find that the spectra are fairly well described by a sum of modified blackbody components (with atomic features superimposed), similar to BHB spectra (Davis & Hubeny 2006). The addition of UV opacity within the disc alone then may not be enough to explain the soft X-ray excess (though it does also depend on the heating profile within the disc); instead, it may be connected to the ability of UV line opacity to launch winds from AGN discs (e.g. Proga, Stone & Kallman 2000; Laor & Davis 2011) and/or the huge change in opacity connected to hydrogen ionization that may be able to change the entire disc structure away from steady-state models (Hameury, Viallet & Lasota 2009).

Constraining the shape of the warm Comptonization component is not easy as it spans the 0.01–1 keV range where interstellar absorption from our own Galaxy obscures our view. Spectral fitting becomes especially degenerate when trying to simultaneously constrain this component along with the hotter coronal component and any residual emission from an outer standard disc (e.g. Jin et al. 2009). Instead, D12 assumed that the emission is ultimately powered by energy release from gravity, with the same form as for the thin disc, but that the dissipation mechanism is only blackbody for radii $R > R_{\rm corona}$, Inwards of this, they assumed that the flow instead emits the accretion energy as a warm or hot Comptonization component. These energy conserving models (OPTXAGNF; D12) give an additional physical constraint on the components, and more importantly, highlight the fundamental parameters of mass and mass accretion rate (for any assumed spin) in setting the overall SED (Jin et al. 2012a,b; Ezhikode et al. 2017). These models reveal a systematic change in the SED that can be modelled by a decrease in $R_{\rm corona}/R_{\rm g}$ (where $R_{\rm g} = GM/c^2$) correlated with an increase in the hot Comptonization power-law spectral index as $L_{\rm bol}/L_{\rm Edd}$ increases (Jin et al. 2012a,b; Ezhikode et al. 2017; see also Shemmer et al. 2006, 2008 and Vasudevan & Fabian 2007, 2009 for the hard X-ray spectral index).

In this paper, we develop a new model that addresses the underlying physics of these changes, where we assume that the flow is completely radially stratified, emitting as a standard disc blackbody from $R_{\rm out}$ to $R_{\rm warm}$, as warm Comptonization from $R_{\rm warm}$ to $R_{\rm hot}$ and then makes a transition to the hard X-ray emitting hot Comptonization component from $R_{\rm hot}$ to $R_{\rm ISCO}$. The warm Comptonization component is optically thick, so we associate this with material in the disc. None the less, the energy does not thermalize to even a modified blackbody, perhaps indicating that significant dissipation takes place within the vertical structure of the disc, rather than being predominantly released in the mid-plane (e.g. Davis et al. 2005). At a radius below $R_{\rm hot}$, the energy is emitted in the hot Comptonization component. This has much lower optical depth, so it is not the disc itself. It could either be a corona above the inner disc, or the disc could truncate, so that the hot material fills the inner region close to the black hole. We show that the observed steepening of the 2–10 keV spectral index with increasing $L_{\rm bol}/L_{\rm Edd}$ can be most easily explained with a true truncation.

We describe the model structure in Section 2, and apply it to observed broad-band spectra of individual AGN in Section 3. We use these data to set some of the model parameters, so that we can predict the entire AGN SED as a function of only mass and mass accretion rate (for a given black hole spin) in Section 4. In Section 5, we show that these models reproduce the observed tight relationship between the UV and X-ray emission in quasars (Lusso & Risaliti 2017) as well as predict a decrease in the fraction of reprocessed optical variability with increasing $L_{\rm bol}/L_{\rm Edd}$ as observed. Thus, this AGN SED model succeeds in describing multiple disparate observational trends, which gives confidence that the assumed geometry captures most major aspects of the source behaviour.

2 OVERALL DISC MODEL

We follow D12 and assume a radial emissivity like Novikov–Thorne (hereafter NT; Novikov & Thorne 1973), defining the flux per unit area at a radius R on the disc as $F_{\rm NT}(R) = \sigma T_{\rm NT}^4(R)$, where $T_{\rm NT}(R)$ is the effective temperature at this radius. Converting to dimensionless units, with $r = R/R_{\rm g}$, $\dot{m} = \dot{M}/\dot{M}_{\rm Edd}$, and $L_{\rm Edd} = \eta \dot{M}_{\rm Edd} c^2$ gives $F_{\rm NT} \propto (\dot{m}/M) r^{-3}$ for $r > >6$. Here, η is a spin-dependent efficiency factor, assumed fixed at 0.057 for a non-spinning black hole throughout this paper.

2.1 Standard disc and warm Comptonization region

In the standard disc region, we assume that the NT emission thermalizes locally either to give a blackbody $B_\nu(T_{\rm NT})$ at the local blackbody temperature, defined from $F_{\rm NT}(R) = \sigma T_{\rm NT}^4(R)$, or that electron scattering within the disc distorts this into a modified disc blackbody spectrum. This can be approximated as a colour temperature corrected blackbody, $B_\nu(f_{\rm col} T_{\rm NT})/f_{\rm col}^4$, where $f_{\rm col}$ depends on the importance of electron scattering compared to true absorption processes, which itself depends on disc temperature, especially close to hydrogen ionization at $\sim 10^4$ K. There are few free electrons below this temperature, so electron scattering is not important, and $f_{\rm col} \sim 1$, whereas above this temperature there are multiple free electrons so $f_{\rm col} > 1$. This effectively shifts the peak of the blackbody over by a factor $f_{\rm col}$, and reduces its norm by a factor $f_{\rm col}^4$ so this gives a shift to higher energy and decrease in normalization in the disc

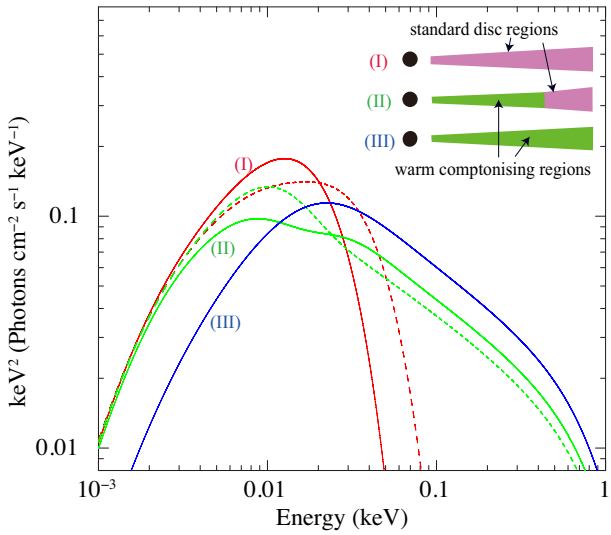

Figure 1. Comparison of spectra for a black hole of $M = 10^8\,M_\odot$ with $\dot{m} = 0.05$. Geometry I shows the NT disc extending down to $R_{\rm ISCO}$ without (red solid) and with (red dashed) colour–temperature correction. Geometry II shows an outer NT disc plus a warm Comptonization region from $r = 40$ down to $r_{\rm ISCO}$. The green solid line shows AGNSED model used in this paper (see Section 2.3) where seed photons are from the underlying cool material in the mid-plane compared to the OPTXAGNF assumption of seed photons from the inner edge of the standard disc (green dashed). Geometry III is complete coverage of the warm Compton region over the entire NT disc (blue), which has lower normalization due to the Compton scattering. We assume a photon index and electron temperature of the warm Comptonizing corona of 2.5 and 0.2 keV, respectively.

spectra from each annulus which onsets at around the hydrogen ionization energy. Thus, the standard disc with this colour–temperature correction always has less UV emission (shortwards of $\sim 10^{15}$ Hz ≈ 2000 Å) than predicted from simple models with $f_{\rm col} = 1$ (D12). Fig. 1 shows a comparison of the standard disc (geometry I) with $f_{\rm col} = 1$ (red solid) to that where $f_{\rm col}(T_{\rm NT})$ is derived from an analytic treatment of the vertical structure of the disc (dashed red line, see also Davis & Hubeny 2006, D12). This clearly shows how the outer disc emission is identical, while the inner disc emission is shifted to higher temperatures/lower luminosities.

Concerning the warm Comptonizing region, the UV data do indeed show a downturn, but this is stronger than predicted by the effect of a changing $f_{\rm col}$ in general. Davis et al. (2007) show that the observed AGN spectra have redder UV slopes than predicted from disc models even including electron scattering. Instead, what is required to fit this UV downturn is that the emission is much more strongly distorted from a blackbody than predicted in the standard disc. While this could be modelled by a larger colour–temperature correction, a shifted blackbody becomes a progressively poorer approximation for the spectrum as $f_{\rm col}$ increases. Hence, we replace $f_{\rm col}$ with a fully Comptonized shape and do not include this factor in our new code as the disc vertical structure is clearly very different to that of Shakura & Sunyaev (1973). Comptonization also gives the possibility to connect the observed downturn in the UV to an upturn seen in the soft X-ray spectra, forming a single component spanning the unobservable EUV range (D12; Mehdipour et al. 2011, 2015). This warm Comptonizing emission could be produced if some fraction of the dissipation takes place higher up in the disc, rather than being concentrated towards the equatorial plane (Czerny et al. 2003; Różańska et al. 2015). Residual emission in the denser disc material on the mid-plane can then act as a source of seed photons, together with the reprocessed emission from illumination from the upper layers of the disc (Petrucci et al. 2018).

Fig. 14 in Davis et al. (2005) shows the predicted (colour temperature corrected) blackbody spectrum of a disc annulus where the vertical dissipation goes with density as in standard disc models, compared to one where the dissipation is arbitrarily changed so that 40 per cent of the power is released in the photosphere (fig. 16 of Davis et al. 2005). The spectrum is strongly Comptonized into a steep tail to higher energies, but clearly contains the imprint of the seed photons as a downturn at low energies. This seed photon temperature is determined both by the intrinsic dissipation in the lower layers of the disc (the remaining 60 per cent of the accretion power in this specific example), and the thermalized flux resulting from irradiation by the Comptonizing upper layers. Both these physical processes give seed photons that are close to the surface temperature predicted by the standard disc dissipation, so the seed photon temperature imprinted on to the steep Comptonized emission is itself close to this temperature (fig. 14 of Davis et al. 2005).

Thus, the expectation is that the seed photon energy should change with radius in the same way as the expected standard disc temperature. D12 discuss this in their appendix, but make the simplifying assumption in OPTXAGNF that this can be approximated as a single Comptonization spectrum with seed photon temperature set by the maximum temperature of the standard disc emission, i.e. $kT_{\rm seed} = kT_{\rm NT}(R_{\rm corona})$. This is adequate if the low-energy part of this component is mostly unobservable due to interstellar absorption. However, there are now data where this region of the spectrum can be seen, motivating a more careful approach. Also, the OPTXAGNF approximation always requires that there is an outer standard disc in order to provide the code with a temperature for the seed photons. This need not be the case in the physical situation envisaged. The warm Comptonization region could instead cover the entire outer disc as its seed photons are from deeper layers of the underlying disc rather than from an external source.

Petrucci et al. (2018) tested a model where the entire optical/UV/soft X-ray flux is from a warm Comptonization region with a slab geometry over the disc. They show that reprocessing in this geometry hardwires the Compton amplification factor A to

$$L_{\rm tot} = AL_{\rm seed} = L_{\rm seed} + L_{\rm diss,warm},$$

where $L_{\rm tot}$, $L_{\rm seed}$, and $L_{\rm diss,\,warm}$ are the total luminosity, seed photon luminosity underneath the Comptonizing skin, and power dissipated in the warm corona, respectively. Their equation (19) with the slab corona entirely covering the disc and large optical depth with complete thermalization gives

$$\frac{L_{\rm diss,warm}}{L_{\rm seed}} = A - 1 = 2\left(1 - \frac{L_{\rm diss,disc}}{L_{\rm seed,tot}}\right) - 1,$$

where $L_{\rm diss,\,disc}$ is the intrinsic dissipation which thermalizes in the disc. If there is no intrinsic dissipation ('passive disc' on the mid-plane; Petrucci et al. 2013, 2018), then all these seed photons are set by thermalization of the warm Compton as $L_{\rm diss,\,disc} = 0$. Thus

$$\frac{L_{\rm diss,warm}}{L_{\rm seed}} = 1$$

hence $L_{\rm seed} = L_{\rm tot}/2$. This is emitted from the same surface area as the standard disc, so thus hardwires the seed photon temperature $T_{\rm seed} \simeq T_{\rm NT}$.

Petrucci et al. (2018) showed that $A = 2$ is equivalent to a photon index of the warm Compton component, $\Gamma_{\rm warm} = 2.5$, which generally gave a good fit to the observed soft X-ray excess component

when combined with a Comptonizing electron temperature $kT_{\rm e,\,warm} \sim 0.2$ keV to give the observed rollover in soft X-rays. Based on this passive disc picture, our new model calculates the Compton emission at each annulus of radius R and width ΔR in the soft Compton region, using the NTHCOMP model (Zdziarski, Johnson & Magdziarz 1996; Życki, Done & Smith 1999) in XSPEC. We set the seed photon temperature to the local disc temperature $T_{\rm NT}(R)$, and set the local luminosity to $\sigma T_{\rm NT}^4(R) \cdot 2\pi R \Delta R \cdot 2$, and sum over all annuli that produce the warm Comptonization. Both photon index and electron temperature are free parameters, assumed to be the same for all the disc annuli that produce the warm Comptonization.

The green solid line in Fig. 1 shows our new version of the warm Comptonization, summed over all radii from $r_{\rm warm} = 40 < r_{\rm out}$ to $r_{\rm ISCO} = 6$ as in geometry II of Fig. 1. We compare this to the OPTXAGNF model for the same parameters (green dashed line), showing the difference in behaviour around the seed photon energy (see also fig. A1b in D12). The blue line in Fig. 1 corresponds instead to the geometry of Petrucci et al. (2018) sketched as geometry III in Fig. 1, i.e. where there is no outer disc so $r_{\rm warm} = r_{\rm out}$. The most noticeable effect is that the normalization of the SED in the optical/UV is reduced. This is important, as it changes the otherwise quite robust relation between the luminosity in some band on the low-energy disc tail and the mass accretion rate. The NT emissivity sets the seed photon temperature and emissivity, but the Comptonization acts like a colour–temperature correction and shifts the entire spectrum to higher energies.

We note here that unlike Petrucci et al. (2018), our new model ties the seed photons for the warm Comptonization to the parameters of the underlying disc, rather than allowing the seed photon temperature to be a free parameter. Both the warm Comptonization and standard disc are optically thick, so we assume that the emission is proportional to $\cos i$, where i is the inclination of the disc.

2.2 Hot Comptonization region

There is also an additional X-ray component that dominates over the soft X-ray excess beyond 1–2 keV, extending up to $kT_{\rm e} \sim 40$–100 keV, with $\tau \sim 1$–2 (Fabian et al. 2015; Lubiński et al. 2016; Petrucci et al. 2018). The low optical depth clearly distinguishes this component from the disc material, and the warm Compton region, so it needs to arise in a different structure. This could either be a corona above a disc, with some fraction of the accretion energy dissipated in this optically thin material, or the optically thick disc could truncate, leaving a true hole in the inner disc. For $\dot{m} \lesssim 0.2$, the hard X-ray photon spectral index is usually $\lesssim 1.9$, i.e. it is flatter than expected even in the limit where all the accretion energy is emitted in the corona. Reprocessing and thermalization of the (assumed isotropic) illuminating flux even by a completely cold, passive disc sets a lower limit on $\Gamma_{\rm hot} \sim 1.9$ (Haardt & Maraschi 1991; Stern et al. 1995; Malzac, Dumont & Mouchet 2005). Hence, we assume that the disc truly truncates at $r_{\rm hot}$ for low $\dot{m}$, as is supported by the lack of strong reflection and lack of strong relativistic smearing these AGN (Matt et al. 2014; Yaqoob et al. 2016; Porquet et al. 2018).

In a truncated disc geometry, the seed photons seen by the hot flow are predominantly from the inner edge of the warm Comptonization region, so these have typical seed photon energy of $T_{\rm NT}(R_{\rm hot}) \cdot \exp(y_{\rm warm})$, where $y_{\rm warm} = 4\tau^2 kT_{\rm e,warm}/m_{\rm e}c^2$ is the Compton y-parameter for the warm Comptonizating corona. We use the XSPEC model NTHCOMP to describe this, with total power

$$L_{\rm hot} = L_{\rm diss,hot} + L_{\rm seed}. \quad (1)$$

(a)The geometry for three emission regeons

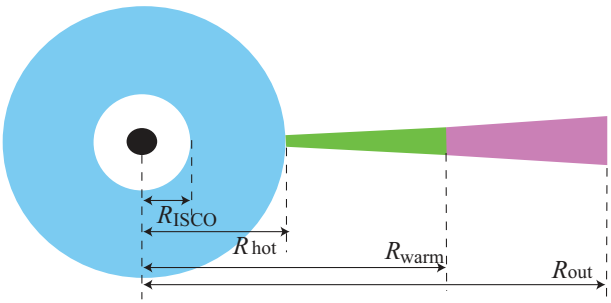

(b)The geometry for hard X-ray reprocess

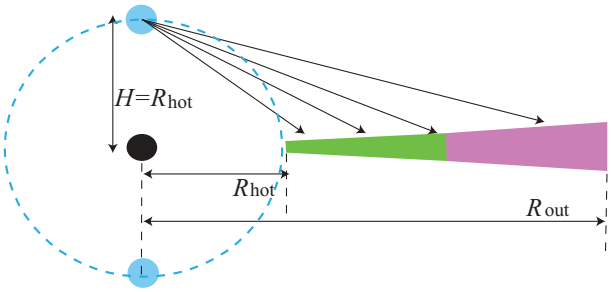

Figure 2. Geometry of the model. (a) The geometry for hot inner flow (blue), warm Compton emission (green), and outer standard disc (magenta). (b) The lamppost geometry used to simplify the calculation of the reprocessed emission.

Here, the inner flow luminosity, $L_{\rm hot}$, is the sum of the dissipated energy from the flow, $L_{\rm diss,\,hot}$, and the seed photon luminosity that is intercepted by the flow, $L_{\rm seed}$.

This gives $L_{\rm diss,\,hot}$ as

$$\begin{aligned} L_{\rm diss,hot} &= 2\int_{R_{\rm ISCO}}^{R_{\rm hot}} F_{\rm NT}(R) 2\pi R {\rm d}R \\ &= 2\int_{R_{\rm ISCO}}^{R_{\rm hot}} \sigma T_{\rm NT}(R)^4 2\pi R {\rm d}R \end{aligned} \quad (2)$$

with the truncated radius $R_{\rm hot}$. This is shown geometrically in Fig. 2(a). Since the X-ray emission is not very optically thick we assume it is isotropic, unlike the disc/warm Comptonization region where we assumed a disc geometry. $L_{\rm seed}$ is the intercepted soft luminosity from both the warm Comptonizing region and the outer disc. This can be calculated assuming a truncated disc/spherical hot flow geometry (Fig. 2a, i.e. a flow scaleheight $H \sim R_{\rm hot}$) as

$$L_{\rm seed} = 2\int_{R_{\rm hot}}^{R_{\rm out}} (F_{\rm NT}(R) + F_{\rm rep}(R)) \frac{\Theta(R)}{\pi} 2\pi R {\rm d}R \quad (3)$$

$$\Theta(R) = \theta_0 - \frac{1}{2}\sin 2\theta_0. \quad (4)$$

Here, $\Theta(R)/\pi$ is the covering fraction of hot flow as seen from the disc at radius $R > R_{\rm hot}$ with $\sin\theta_0 = H/R$, and $F_{\rm NT}(R) + F_{\rm rep}(R)$ is the flux from the warm Comptonized and/or outer disc including reprocessing (discussed in the following section).

We caution that there can be many other factors that influence $L_{\rm seed}$ e.g. overlap of the disc and hot flow (Zdziarski, Lubiński & Smith 1999) and/or any radial/vertical gradient in the structure of the hot flow. None the less, we start from the simplest possible assumption which is a spherical, homogeneous source with

$H = R_{\rm hot}$ but we leave H as a parameter in the following equations so that it can be used as a tuning parameter for alternative geometries by changing the seed photons intercepted by the source. Smaller H gives a smaller solid angle, so fewer seed photons and harder spectral indices, but has no effect on $R_{\rm hot}$ as this is set by the energetics.

2.3 Modelling reprocessing

The assumed geometry shown in Fig. 2(a) has some fraction of the hot Comptonization illuminating the warm Comptonization and cool outer disc regions. We include this self-consistently, so that the irradiating flux increases the local flux above that given by the intrinsic $\dot{M}$. Though our geometry assumes that the hot corona is an extended source, with $H \sim R_{\rm hot}$ as above (see Fig. 2a), Gardner & Done (2017) show that illumination from an extended source can be well approximated by a point source at height H on the spin axis (lampppost, Fig. 2b). We thus utilized the lamppost geometry for the hot inner flow to calculate the reprocessed flux as it is simpler than integrating over an extended source.

The reprocessed flux for a flat disc at a radius R is then written as

$$F_{\rm rep}(R) = \frac{\frac{1}{2}L_{\rm hot}}{4\pi(R^2+H^2)}\frac{H}{\sqrt{R^2+H^2}}(1-a) = \frac{3GM\dot{M}}{8\pi R^3}\frac{2L_{\rm hot}}{\dot{M}c^2}\frac{H}{6R_{\rm g}}(1-a)\left[1+\left(\frac{H}{R}\right)^2\right]^{-3/2}, \quad (5)$$

where a is the reflection albedo. Hence, the local flux at radius $R(>R_{\rm hot})$ is $\sigma T_{\rm eff}(R)^4 = F_{\rm NT}(R) + F_{\rm rep}(R)$. Both $F_{\rm NT}(R)$ and $F_{\rm rep}(R)$ depend on radius as R^{-3} for $R \gg R_{\rm g}$, thus the effect of the reprocessing is basically to increase the flux across both the standard and warm Comptonized disc by the same factor that is of the order of $1 + H/6R_{\rm g}$. Hence, a larger X-ray source increases the fraction of X-ray power that illuminates the disc, as well as increasing the fraction of bolometric power that is dissipated in the X-ray region via the change in $R_{\rm hot} = H$.

Fig. 3 shows a comparison of example spectra with (solid) and without (dashed) reprocessing for a black hole of $10^8\,{\rm M}_\odot$ with $\dot{m} = 0.05$ (blue) and 0.5 (red). We set $L_{\rm diss,\,hot} = 0.02L_{\rm Edd}$ and $kT_{\rm e,hot} = 100$ keV for both, which implies $r_{\rm hot} = 23$ and 9 for $\dot{m} = 0.05$ and 0.5, respectively. $\Gamma_{\rm hot}$ is set to be 1.8 and 2.2 for $\dot{m} = 0.05$ and 0.5, respectively. We also include a warm Comptonization region with $kT_{\rm e,\,warm} = 0.2$ keV and $\Gamma_{\rm warm} = 2.5$. Fig. 3(a) shows models where the warm Comptonization region extends from $r_{\rm hot}$ to $r_{\rm warm} = 2r_{\rm hot}$, so that there is a standard outer disc region from $r_{\rm warm}$ to $r_{\rm out}$, while Fig. 3(b) shows the alternative geometry where the warm Comptonization extends over the entire outer disc, i.e. $r_{\rm warm} = r_{\rm out}$.

The lower panels of Figs 3(a) and (b) highlight the effect of reprocessing by showing the ratio of the spectra including reprocessing to the intrinsic emission. Reprocessing makes a larger fraction of the optical emission for the lower $\dot{m}$, as here the ratio of the X-ray flux to optical disc emission is much larger, and the larger size scale of the X-ray source means that a larger fraction of the X-ray emission is intercepted by the disc. The difference is most marked around the maximum in the SED as the flux increase from reprocessing is enhanced by the associated temperature increase in disc or seed photon energy.

We call this new model AGNSED, and in the Appendix define all the parameters. The model is publicly available for use in the XSPEC spectral fitting package. We also release a simplified model QSOSED where many of the parameters are fixed. This is more suitable for fitting fainter objects such as distant quasars, where the signal-to-noise ratio is limited.

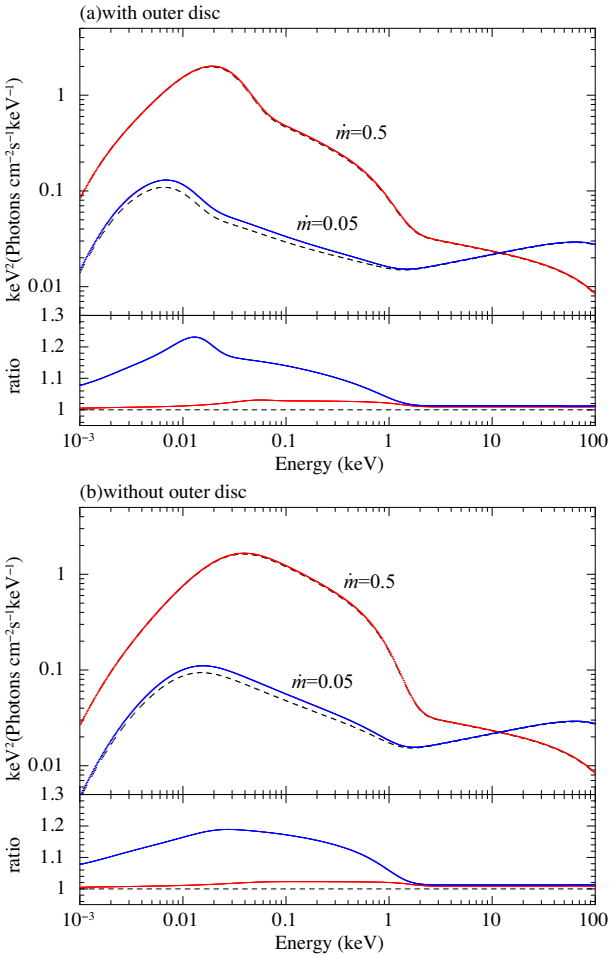

Figure 3. Comparison of spectra with (solid) and without (dashed) reprocessing for a black hole of $M = 10^8\,{\rm M}_\odot$ with $\dot{m} = 0.05$ (blue) and 0.5 (red) at a distance 100 Mpc. The values of $kT_{\rm e,\,warm}$, $\Gamma_{\rm warm}$, $kT_{\rm e,\,hot}$, and $L_{\rm diss,\,hot}$ are assumed to be 0.2 keV, 2.5, 100 keV, and $0.02L_{\rm Edd}$, respectively. The values of $\Gamma_{\rm hot}$ are assumed to be 1.8 and 2.2 for $\dot{m} = 0.05$ and 0.5, respectively. Panel (a) and (b) correspond to with and without outer standard disc, respectively. In panel (a), $r_{\rm warm}$ is set to be $2r_{\rm hot}$. Ratios of reprocessed to intrinsic emission are also shown at each energy.

3 APPLICATION TO OBSERVED SPECTRA

We apply AGNSED to a small sample of AGN, spanning a wide range of $\dot{m}$, chosen to have good multiwavelength data. We select NGC 5548 ($\dot{m} \sim 0.03$; Mehdipour et al. 2015) and Mrk 509 ($\dot{m} \sim 0.1$; Mehdipour et al. 2011), for which big multiwavelength observation campaigns have been performed. Based on the long-term observations with the Reflection Grating Spectrometers (RGS) on board *XMM–Newton*, their intrinsic absorption were extremely well determined (Detmers et al. 2011; Mehdipour et al. 2011, 2015) and removed from the SEDs. In this paper, we fit the best estimate of the continuum spectra from these AGN, deconvolved from the instrument response, and corrected for reddening and absorption. We read the resulting flux files into XSPEC using the FLX2XSP command. These deconvolved data were kindly provided by M. Mehdipour. In order to apply the model to higher $\dot{m}$ AGN, we select PG 1115 + 407

Table 1. System parameters to calculate each spectrum. Comoving radial distance D and luminosity distance D_L is calculated based on $H_0 = 69.6\,\mathrm{km\,s^{-1}\,Mpc^{-1}}$ and $\Omega_M = 0.286$ with flat universe (Wright 2006).

		NGC 5548	Mrk 509	PG 1115 + 407
z		0.017 175	0.034 397	0.154 338
D	Mpc	73.7	147.1	642.1
D_L	Mpc	75.0	152.1	741.2
M	$10^7\,M_\odot$	2–6	10–30	4.6–14
Eddington ratio		∼0.03	∼0.1	∼0.4
Observation		2013	2009	2002
Reference		(1), (2)	(3), (4)	(5), (6)

Notes. (1) Kaastra et al. (2014); (2) Mehdipour et al. (2015); (3) Kaastra et al. (2011a); (4) Mehdipour et al. (2011); (5) Jin et al. (2012a) and (6) Jin et al. (2012b).

from 51 AGN sample analysed by Jin et al. (2012a). This object has little intrinsic absorption with $\dot{m} \sim 0.4$ (Jin et al. 2012a), and emission from the host galaxy is negligible in band of the optical monitor (OM) onboard *XMM–Newton* (Ezhikode et al. 2017).

The system parameters for each AGN are given in Table 1. We fit all three SED with AGNSED with $i = 45^\circ$ and limit the mass to the uncertainty range given in Table 1. The outer disc radius, r_{out}, is initially set to equal to the self-gravity r_{sg} (Laor & Netzer 1989).

3.1 NGC 5548: $\dot{m} \sim 0.03$

The Seyfert-1 galaxy NGC 5548 is one of the most widely studied nearby AGN, with well-constrained mass $(2–6)\times10^7\,M_\odot$. There was a multiwavelength campaign on this object in 2012–2014 (e.g. Kaastra et al. 2014), and the broad-band spectra were analysed by Mehdipour et al. (2015). We use the data from summer 2013 shown in fig. 10 of Mehdipour et al. (2015), which include data points from NuSTAR, INTEGRAL, RGS, and the European Photon Imaging Camera (EPIC-pn) on *XMM–Newton*, the Cosmic Origins Spectrograph (COS) on the *Hubble Space Telescope* (*HST*), the UltraViolet and Optical Telescope (UVOT) on *Swift*, and from two ground-based optical observatories: the Wise Observatory (WO) and the Observatorio Cerro Armazones (OCA). During this campaign, there are multiple absorption systems seen in the X-ray (Kaastra et al. 2014; Mehdipour et al. 2015; Cappi et al. 2016), which have been removed from our data using the best-fitting modelling of the RGS spectra (Mehdipour et al. 2015). None the less, there is some uncertainty associated with this, which affects the determination of the intrinsic soft X-ray spectrum.

There is also strong host galaxy contamination in the optical, so this was removed (fig. 10; Mehdipour et al. 2015) to isolate the AGN emission. The resulting optical/UV continuum is rather blue, and cannot easily be fit with any disc blackbody based model, either a standard disc or warm Comptonized one. Mehdipour et al. (2015) fit this by a single, warm Comptonization region, using blackbody (not disc blackbody) seed photons in order to get such a steeply rising optical/UV continuum. It seems more likely that this is a consequence of a slight oversubtraction of the host galaxy, so we ignore the V and I band continuum points in the fit. The X-ray emission is extremely bright compared to the optical/UV, and very hard.

We then fit the data with AGNSED, including three emission regions. There is a clear iron line in the X-ray data, but the accompanying Compton hump is rather weak (Ursini et al. 2015; Cappi et al. 2016), so this line probably originates in optically thin material in the BLR (Yaqoob et al. 2001; Brenneman et al. 2012; Ursini et al. 2015).

Table 2. The best estimated parameters.

		NGC 5548	Mrk 509	PG1115 + 407
		With outer disc		
N_H	$\mathrm{cm^{-2}}$	–	–	2.2×10^{20}
Mass	$M_\odot$	5.5×10^7	1.0×10^8	1.0×10^8
$\dot{m}$		0.027	0.10	0.40
Γ_{warm}		2.28	2.36	3.06
$kT_{e,warm}$	keV	0.17	0.20	0.50
Γ_{hot}		1.60	1.96	2.14
$kT_{e,hot}$	keV	39	100†	100†
$L_{diss,\,hot}$	L_{Edd}	0.017	0.038	0.026
L_{hot}	L_{Edd}	(0.018)	(0.042)	(0.040)
		Size scales		
r_{hot}		(43)*	(21)*	(9.8)*
r_{warm}		151	40	35
r_{out}		282	(780)*	(1416)*
		Characteristic temperatures		
$T(R_{hot})$	K	$(2.9\times10^4$	5.4×10^4	$1.0\times10^5)$*
$T(R_{warm})$	K	$(1.3\times10^4$	3.7×10^4	$5.6\times10^4)$*
$T(R_{out})$	K	$(8.0\times10^3$	4.6×10^3	$4.1\times10^3)$*
χ^2_ν(dof)		1.65(1097)‡	1.44(370)‡	1.64(184)
		Without outer disc		
N_H	$\mathrm{cm^{-2}}$	–	–	3.1×10^{20}
mass	$M_\odot$	6.0×10^7 **	3.0×10^8 **	1.3×10^8
$\dot{m}$		0.024	0.041	0.46
Γ_{warm}		2.39	2.59	3.35
$kT_{e,warm}$	keV	0.18	0.28	0.52
Γ_{hot}		1.61	1.87	2.21
$kT_{e,hot}$	keV	33	100†	100†
$L_{diss,\,hot}$	L_{Edd}	0.016	0.013	0.021
L_{hot}	L_{Edd}	(0.017)	(0.015)	(0.038)
		Size scales		
r_{hot}		(49)*	(19)*	(9.1)*
$r_{warm,\,out}$		1000**	(407)*	(1432)*
		Characteristic temperatures		
$T(R_{hot})$	K	$(2.5\times10^4$	3.4×10^4	$9.9\times10^4)$*
$T(R_{warm,\,out})$	K	3.0×10^3	4.4×10^3	$4.0\times10^3)$*
χ^2_ν(dof)		2.11(1098)‡	2.01(371)‡	1.77(185)

Notes †Electron temperature of the hot flow is fixed at 100 keV.
*Values in the parenthesis are internally calculated based on the other parameters.
‡The absolute values of χ^2_ν are not meaningful for deconvolved spectral fit. They are shown only for reference to compare the fit goodness between with and without outer disc. Reflection components are modelled by a single Gaussian and GSMOOTH*PEXMON for NGC 5548 and Mrk 509, respectively.
**The values are limited by upper limit of parameters.

We model this simply by including a Gaussian in the fit. The model overpredicts the optical data for $r_{out} = r_{sg} = 880$ for $\dot{m} \sim 0.03$. This could again indicate a slight oversubtraction of the host galaxy from our data, but we are able to fit by allowing the outer disc radius to be a free parameter, giving $r_{out} = 280$. The overall continuum shape and luminosity is then fairly well reproduced by AGNSED with $M = 5.5\times10^7\,M_\odot$ and $\dot{m} \simeq 0.03$. The best-fitting parameters are shown in Table 2, and the best-fitting model is overlaid on the deconvolved data points in Fig. 4(a). The estimated Γ_{warm} of 2.28 is harder than the passive disc prediction of 2.5 and may indicate patchy corona as suggested by Petrucci et al. (2018). We discuss this in more detail in Section 4.3.

We also try to reproduce the data without any standard outer disc component, as in Mehdipour et al. (2015) and Petrucci et al. (2018). However, in our fit the seed photon energy is not a free parameter, but is set at the underlying disc temperature from reprocessing. The UV data are clearly in tension with this, as they show a stronger

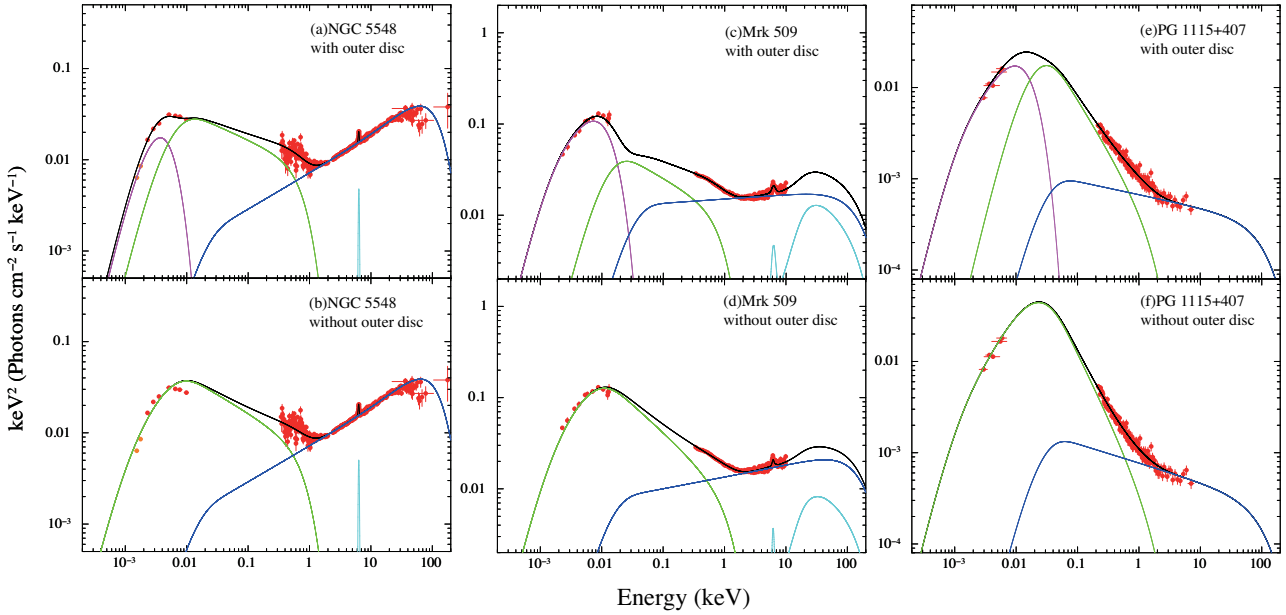

Figure 4. The best estimated models overlaid on the data set of NGC 5548 (fig. 10; Mehdipour et al. 2015), Mrk 509 (fig. 12; Mehdipour et al. 2011), and PG 1115 + 407 (Jin et al. 2012a,b). The outer disc emission, the warm Compton component, and the hard Compton component are shown in magenta, green, and blue, respectively. Panels (a), (b), (c), (d), (e), and (f) correspond to NGC 5548 with and without outer disc, Mrk 509 with and without outer disc and PG 1115 + 407 with and without outer disc, respectively.

downturn than predicted by the warm Comptonization models with seed photon energy set by the underlying disc area from reprocessing. A warm Comptonization region covering the outer disc also changes some other aspects of the fit. The lower normalization in the optical/UV (see Fig. 2, geometry III) means that the same parameters of mass and mass accretion rate underpredict the optical data.

Including the warm layer across all of the disc means that there should be an increase in $(M\dot{M})^{2/3}$ to compensate for the decrease in normalization from Comptonization. However, the observed bolometric luminosity $L_{\rm bol} = \eta \dot{M} c^2$ that is fairly well constrained by the data. Hence, the only possibility to increase the optical emission is to increase the mass. This now pegs at the upper limit, giving a slight decrease in $\dot{m} \propto \dot{M}/M$. The outer radius is now not constrained from the data, with little change in goodness of fit from $r_{\rm out} = 10^3$ to 10^5, so we set this back to the self-gravity radius. We show the best fit with these assumptions in Fig. 4(b), and tabulate the parameters in Table 2.

In order to explain the optical data points that peak energy at 8–10 eV with entire warm Comptonization, black hole mass needs to be as large as 1×10^8 M$_\odot$ with $\dot{m} \sim 0.01$ and $L_{\rm diss,hot} \sim 0.01\, L_{\rm Edd}$. This clearly exceeds the reasonable range of black hole mass of NGC 5548. Hence, we conclude there is most likely a standard outer disc in NGC 5548.

3.2 Mrk509: $\dot{m} \sim 0.1$

Mrk 509 is the nearby Seyfert-1/quasar, and is one of the first objects in which the soft X-ray excess was discovered (Singh, Garmire & Nousek 1985). There was a large multiwavelength campaign on this object (Kaastra et al. 2011a,b), with simultaneous optical-UV and X-ray monitoring from *XMM–Newton*'s OM and EPIC-pn together with the *HST*/COS and archival observation by the Far Ultraviolet Spectroscopic Explorer (FUSE) (Mehdipour et al. 2011). As in Mehdipour et al. (2015), they fit the continuum SED without any outer disc emission, just using a warm (0.2 keV) optically thick ($\tau \sim 17$) Comptonization component with free seed photon temperature, together with a hard ($\Gamma \sim 1.9$) power-law X-ray continuum.

There is a clear iron line in the X-ray spectrum, together with a Compton hump, so we include this in the model using GSMOOTH ∗ PEXMON (Nandra et al. 2007). The best-fitting model is shown in Fig. 4(c) and detailed in Table 2. The data are then well fitted with our three-component AGNSED continuum (i.e. including an outer disc) for a black hole mass of 1×10^8 M$_\odot$ with $\dot{m} = 0.1$. The transition radius from the outer disc to warm Comptonized disc is around $r_{\rm warm} \simeq 40$, while the observed X-ray emission requires $r_{\rm hot} = 21$.

We also try a fit where the entire outer disc is covered by the warm Comptonization (Fig. 4d). This is statistically worse than the model with an outer standard disc, but unlike NGC 5548, the data match fairly well to the model around the UV peak. This model also gives $\Gamma_{\rm warm} \simeq 2.6$, consistent with a passive disc.

3.3 PG 1115+407: $\dot{m} \sim 0.4$

PG 1115 + 407 is a NLS1 galaxy with mass from single epoch spectra of 4.6×10^7 M$_\odot$ using historical data with full width at half-maximum (FWHM) H β of 1720 km s^{-1} (Porquet et al. 2004), or 9.1×10^7 M$_\odot$ with the (narrow line subtracted) Sloan Digital Sky Survey (SDSS) FWHM H β of 2310 km s^{-1} (Jin et al. 2012a). Hence, we assumed a black hole mass range of $(0.46–1.4) \times 10^8$ M$_\odot$, including 0.2 dex uncertainty on the SDSS limit (Table 1). We re-analysed the same data set shown in Jin et al. (2012a,b) by concentrating on *XMM*/OM and *XMM*/EPIC-pn data alone since the SDSS data points were not simultaneous with the *XMM* observation. We fit the data with TBABS∗REDDEN∗AGNSED, where TBABS is used with Anders & Ebihara (1982) abundance and $E(B-V)$ is tied to $N_{\rm H} \cdot (1.7 \times 10^{-22})$ as was done in Jin et al. (2012a). The observation is only 9.4 ks, and the spectrum is steep. This makes it difficult to

constrain any reflection component so this is not included in the model.

As shown in Table 2, the model with an outer disc fits the data well, and $N_{\rm H}$ of 2.2×10^{20} cm^{-2} is consistent with galactic absorption of $(1.5–1.9) \times 10^{20}$ cm^{-2} (Dickey & Lockman 1990; Kalberla et al. 2005). The unabsorbed SED derived from this best-fitting model is shown in Fig. 4(e). Black hole mass is estimated as $M = 1.0 \times 10^8$ M$_\odot$ with $\dot{m} = 0.4$. The size of the hot corona is $r_{\rm hot} = 9.8$, which is much smaller than for the lower $\dot{m}$ AGN. For the warm Comptonizing region, while $r_{\rm warm}$ is similar to that of Mrk 509, $\Gamma_{\rm warm}$ is much steeper at ∼3.1. This most likely indicates that there is some intrinsic disc power dissipated underneath the warm corona rather than a completely passive disc. We compare this to models where the entire disc is dominated by the warm Compton component. The fit results are shown in Table 2 and Fig. 4(f). The fit is slightly worse in terms of χ^2_ν, and has slightly larger absorption at $N_{\rm H} = 3.1 \times 10^{20}$cm^{-2}.

4 FULL AGN BROAD-BAND SPECTRAL MODEL

In this section, we evaluate the results of fitting AGNSED to the observed SED of NGC 5548 ($\dot{m} \sim 0.03$), Mrk 509 ($\dot{m} \sim 0.1$), and PG 1115 + 407 ($\dot{m} \sim 0.4$), and use these, together with other results in the literature, to build a full SED picture where the only free parameters are M and $\dot{m}$.

4.1 Existence of an outer standard disc component

All the AGN in Section 3 are consistent with AGNSED of three components, where there is an outer disc, together with warm Comptonizing region and hot corona, powered by NT emissivity for a low spin black hole. This is always a better fit than assuming $r_{\rm warm} = r_{\rm out,}$ i.e. a model where the warm Comptonization region extends over the entire outer disc, although there are several uncertainties, e.g. on the inclination and absorption corrections. Our model is different to that fit by Mehdipour et al. (2015) and Petrucci et al. (2018), where the optical/UV data are from the warm Comptonization component alone. This difference is due to our assumption that the warm Comptonization is intrinsically linked to an NT disc. The data do fit just as well to an unconstrained warm Comptonization component as this has the same optical/UV shape as a standard disc (see Fig. 1 geometry III). However, we have additional requirements on the luminosity and seed photon temperature from our assumed NT emissivity. The optically thick, warm Comptonization thus suppresses the flux below that predicted by the outer disc, so these models require a higher M and/or higher absolute mass accretion rate, $\dot{M}$, but the latter is fairly well constrained by the observed bolometric luminosity from the broad-band spectra.

A larger $\dot{M}$ through the outer disc could fit the data if this is counteracted by strong energy losses, e.g. if the system powers a UV line-driven wind (Laor & Davis 2014). However, it seems somewhat fine tuned that these wind losses (which vary with M and $\dot{M}$) would be always able to almost exactly compensate for the extra power predicted by NT emissivity that assumes a constant $\dot{M}$ with radius. Similarly, high black hole spin would give higher luminosity for a given $\dot{M}$ through the outer disc, which can overpredict the total luminosity unless this is mainly dissipated in the unobservable EUV bandpass. Again, this seems fine tuned. The simplest solution is that we are seeing evidence for an outer disc whose properties are like the standard disc, and that the wind losses are small, and spin is low.

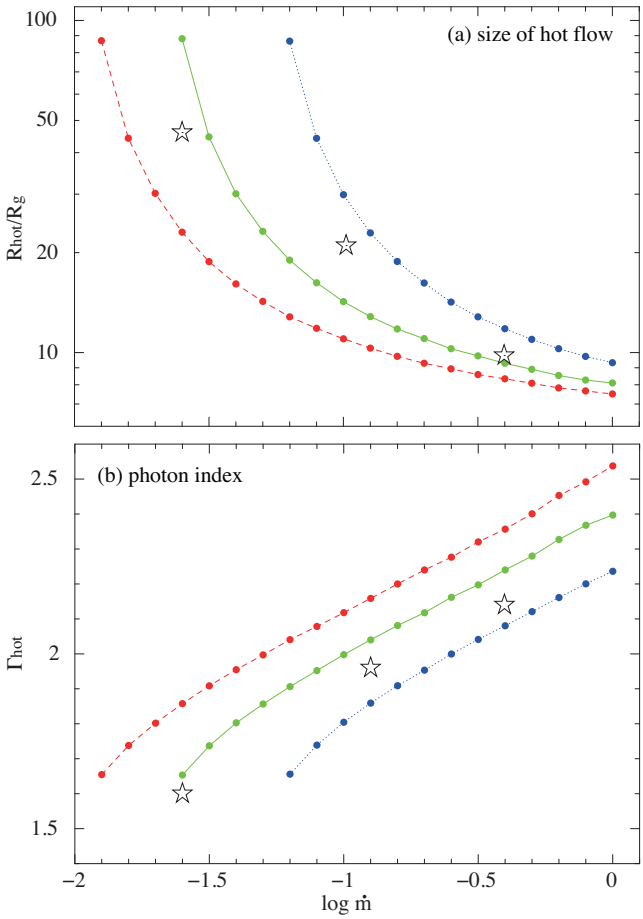

Figure 5. Radius of the hot inner flow, $r_{\rm hot}$, (a) and photon index of the hot Compton component, $\Gamma_{\rm hot,}$ (b) are plotted against $\log \dot{m}$. The values are calculated assuming a fixed $L_{\rm diss,\,hot}$ of 0.01 $L_{\rm Edd}$ (dashed red line), 0.02 $L_{\rm Edd}$ (solid green line), and 0.05 $L_{\rm Edd}$ (dotted blue line). The spectral index is calculated with reprocess. The observed values of $r_{\rm hot}$ and $\Gamma_{\rm hot}$ for Mrk 509, NGC 5548, and PG 1115 + 407 are shown with open stars.

4.2 Hot coronal emission

As shown in Table 2, the observed power dissipated in the hot inner flow is $L_{\rm diss,\,hot} = 0.02–0.04\,L_{\rm Edd}$ in our three AGN with different $\dot{m}$. This is also seen in the sample of 50 AGN in Jin et al. (2012a). These have different masses and $\dot{m}$, but the X-ray luminosities are all the same within a factor of 2–3 when the SEDs are stacked into three groups of low, medium, and high $\dot{m}$ and referenced to the same black hole mass (fig. 8b in D12).

4.2.1 Truncated disc and inner hot flow geometry

In our model, the approximately fixed value for $L_{\rm diss,\,hot}$ measured from the data then determines $r_{\rm hot}$ from the NT emissivity. For a total $\dot{m} \sim 0.03$, most of the entire flow energy is needed to power the hard X-ray region, thus $r_{\rm hot}$ is large. Conversely, for $\dot{m} \sim 0.4$, only a very small fraction of the available power is needed to make the hard X-ray flux, so $r_{\rm hot}$ is small. Fig. 5(a) shows how the value of $r_{\rm hot}$ decreases as a function of increasing $\dot{m}$ in models where $L_{\rm diss,\,hot}$ is fixed at 0.01 $L_{\rm Edd}$ (dashed red), 0.02 $L_{\rm Edd}$ (solid green), and 0.05 $L_{\rm Edd}$ (dotted blue). The open stars show the values measured from fitting to the data scatter around the green line, consistent with constant $L_{\rm diss,hot} = 0.02\,L_{\rm Edd}$, especially considering the

uncertainties on mass determination. The predicted decrease in size scale of the X-ray source with increasing $L_{\rm bol}/L_{\rm Edd}$ is compatible with the observations that the X-ray variability time-scale decreases with increasing $L_{\rm bol}/L_{\rm Edd}$ (McHardy et al. 2006).

We also calculate the self-consistent spectral index, $\Gamma_{\rm hot}$, for the flow from equation 14 in Beloborodov (1999) as

$$\Gamma_{\rm hot} = \frac{7}{3}\left(\frac{L_{\rm diss,hot}}{L_{\rm seed}}\right)^{-0.1}. \quad (6)$$

With the geometry of the truncated inner flow shown in Fig. 2(a), $L_{\rm diss,\,hot}$ and $L_{\rm seed}$ are calculated via equations (2) and (3), respectively. Fig. 5(b) shows the resulting $\Gamma_{\rm hot}$ assuming $L_{\rm diss,\,hot}$ at 0.01 $L_{\rm Edd}$ (dashed red), 0.02 $L_{\rm Edd}$ (solid green), and 0.05 $L_{\rm Edd}$ (dotted blue). The data (open stars) are in good agreement with the truncated disc geometry for $L_{\rm diss,hot} = 0.02\,L_{\rm Edd}$. The observed spectral indices are then consistent with a truncated disc geometry across the entire range of $\dot{m}$ considered here. This is surprising, especially at high $\dot{m}$, where the corona is more generally drawn as either X-ray hot plasma over the inner disc or as a lamppost (compact source on the spin axis of the black hole). We explore untruncated disc geometries in Sections 4.2.2 and 4.2.3.

4.2.2 *Passive disc and inner hot corona geometry*

Instead of the truncated disc and inner hot flow, there can be an inner disc corona extending down to $r_{\rm ISCO}$. The inner disc corona can be characterized by the fraction, f, of power dissipated in the corona with the remaining cooler disc material in the mid-plane (Svensson & Zdziarski 1994).

We first assume a maximal corona, with $f = 1$ extending over the inner disc from $r_{\rm hot}$ to $r_{\rm ISCO}$, i.e. a total power dissipated in the corona of $L_{\rm diss,\,hot} = 0.02 L_{\rm Edd}$ with a passive disc on the mid-plane. The difference between this and the truncated disc geometry (Section 4.2.1) is that the inner disc on the mid-plane will intercept half of the X-ray emission from the corona for an isotropic source. The albedo, a, determines how much of the illuminating flux can be reflected. The reflected fraction at low energies depends strongly on the ionization of the disc, but photons above ∼50–100 keV cannot be reflected elastically due to Compton downscattering. This gives a maximum albedo for completely ionized (most reflective) material and this value depends on spectral shape. We evaluate this for a Compton spectrum (NTHCOMP) with $kT_{\rm e} = 100$ keV and different values of Γ and calculate the reflection albedo using IREFLECT (Magdziarz & Zdziarski 1995) with $\xi = 10^6$ erg s^{-1}cm. We choose this rather than the newer reflection models such as RELXILL as IREFLECT calculates only the reflected emission; the emission lines and recombination continua will add to the thermalized flux in making soft seed photons. This gives $a_{\rm max} = 0.55$–0.81 for $\Gamma = 1.5$–2.3.

On the other hand, the seed photon power from reprocessing in the corona region results in

$$\frac{L_{\rm diss,hot}}{L_{\rm seed}} = \frac{f}{1-\frac{1}{2}f-\frac{1}{2}fa} = \frac{2}{1-a}$$

with maximal corona, $f = 1$ (see equation 3a in Haardt & Maraschi 1993). This indicates

$$\Gamma_{\rm hot} = \frac{7}{3}\left(\frac{2}{1-a}\right)^{-0.1}$$

via equation (6). Thus, $a_{\rm max}$ and $\Gamma_{\rm hot,\,min}$ are self-consistently determined as $a_{\rm max} \sim 0.7$ and $\Gamma_{\rm hot,\,min} \sim 1.9$ for an inner disc corona geometry. In Fig. 6, which shows the truncated disc results as a baseline model (green solid line) together with the data (open stars) from Fig. 5, we plot $\Gamma_{\rm hot}$ as a horizontal dotted black line. This horizontal dotted black line shows this minimum photon index. The observed $\Gamma_{\rm hot}$ for Mrk 509 sits on this lower limit, so can be explained also by this geometry. PG 1115 + 407 is somewhat steeper at $\Gamma_{\rm hot} = 2.2$, which can also be explained by this geometry for $a = 0.3 (< a_{\rm max})$. However, NGC 5548 and other AGN with $\Gamma_{\rm hot} < 1.9$ require a more photon starved geometry.

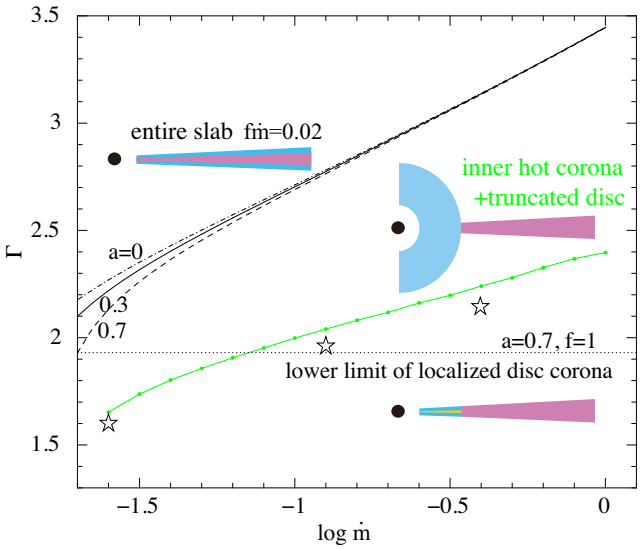

Figure 6. Same as Fig. 5(b), but expected values of $\Gamma_{\rm hot}$ for slab geometry with $L_{\rm diss,hot} = 0.02\,L_{\rm Edd}$ (i.e. $f\dot{m} = 0.02$ with the fraction of power dissipated in the corona, f) are shown in black lines, together with the observed values of $\Gamma_{\rm hot}$ for Mrk 509, NGC 5548 and PG 1115 + 407 (open stars) and $\Gamma_{\rm hot}$ for truncated disc geometry with $L_{\rm diss,hot} = 0.02\,L_{\rm Edd}$ (solid green). Albedo is assumed to be $a = 0$ (dash–dotted), 0.3 (solid), and 0.7 (dash). Horizontal dotted straight lines represent the lower limit of Γ under an assumption of localized slab corona with maximal albedo, $a = 0.7$ and by assuming 'passive disc' underneath the corona, i.e. $f = 1$.

4.2.3 *Entire slab hot corona*

The value of $\Gamma_{\rm hot}$ becomes larger if there is intrinsic disc power (i.e. $f < 1$), which adds to the seed photons in the local slab geometry. This requires larger $r_{\rm hot}$ to keep the same observed $L_{\rm diss,\,hot}/L_{\rm Edd}$. The most extreme case is where the corona extends over the entire optically thick disc so that f is constant with radius. For such an entire slab geometry, the seed photons are given by equation (3a) in Haardt & Maraschi (1993) as

$$\frac{L_{\rm seed}}{L_{\rm Edd}} = \left(1-\frac{1}{2}f-\frac{1}{2}fa\right)\dot{m}.$$

In this geometry, the hard X-ray dissipation of $L_{\rm diss,hot}/L_{\rm Edd} = f\dot{m} = 0.02$ implies $f = 0.02/\dot{m}$. We use this in the equation above to calculate $L_{\rm diss,\,hot}/L_{\rm seed}$ as

$$\frac{L_{\rm diss,hot}}{L_{\rm seed}} = \frac{f\dot{m}}{(1-\frac{1}{2}f-\frac{1}{2}fa)\dot{m}} = \frac{2}{100\dot{m}-1-a}$$

and hence derive the spectral index via equation (6). We plot these in Fig. 6 for three values of the albedo namely $a = 0$ (dotted), 0.3 (solid), and 0.7 (dashed). These always give much steeper $\Gamma_{\rm hot}$ than observed. Fig. 6 shows that steep spectra of $\Gamma_{\rm hot} \simeq 3.1$–$3.4$ are predicted for $\log\dot{m} = -0.6 \sim 0$ while the observed photon indices are usually harder as 1.7–2.4 (e.g. from 55 samples in Jin et al.

2012a). For lowest $\dot{m}$, $\Gamma_{\rm hot}$ is still as large as 1.9. Thus, the entire slab for the hot Comptonization component is quite unlikely for both high and low $\dot{m}$. This problem is discussed in detail also e.g. by Stern et al. (1995), Malzac et al. (2005), and Poutanen, Veledina & Zdziarski (2018) for the case of BHBs in the low/hard state. The problem is even more marked for AGN as the disc seed photons are at lower energies, making Compton cooling more efficient and leading to steeper predicted photon indices (Haardt & Maraschi 1993).

4.2.4 Summary of constraints on the geometry of the hot corona

To summarize, the data at $\dot{m} \leq 0.1$ have $\Gamma_{\rm hot} < 1.9$ that is incompatible with a disc-corona geometry even in the limit where all the power is dissipated in the corona. Spectra at higher $\dot{m} \geq 0.1$ have spectra that can be produced in an inner disc-corona geometry, but these require some fine tuning in order to produce the spectral indices observed. By contrast, the truncated disc/hot inner flow geometry can predict the behaviour of the spectral index over the entire range of $\dot{m}$, making it likely that this geometry is continued across all $L_{\rm bol}/L_{\rm Edd}$.

4.3 Warm Comptonization region

The warm Comptonization region extends from $r_{\rm hot}$ to an outer radius $r_{\rm warm} \lesssim r_{\rm out}$. Ideas that associate this with the changing vertical structure of a disc due to the importance of atomic opacities predict that the warm Comptonization region should onset at an approximately fixed temperature. One attractive idea is that each annulus of the disc that is at the same temperature as an O star would be modified by a UV line-driven wind (Laor & Davis 2014). The maximum disc temperature considering these wind losses is (2–8)$\times$ 10^4 K in their models, which is similar to the range seen here for the onset of the warm Comptonization of (1–6)$\times$ 10^4 K. Thus, it is possible that the onset of warm Comptonization does link to the changing disc structure induced by UV opacities, though strong wind losses such as those predicted by Laor & Davis (2014) are ruled out by the observed efficiencies.

This overprediction of wind losses is probably linked to the assumption in Laor & Davis (2014) that there is only a disc, with no hard X-ray emission that will strongly suppress UV line driving by overionization (Proga et al. 2000). It seems plausible that the UV bright disc launches a UV-driven disc wind, but that this becomes ionized as it rises up and is exposed to the X-ray source. The failed wind falls back down, impacting the disc, leading to shock heating of the photosphere, making the warm Comptonization region. There are no calculations of this at the current time, but we expect that the extent of the failed wind will depend on the level of X-ray ionization. This is clearly larger for lower $\dot{m}$. Guided by the fits to the individual objects above, we tie the size scale, $r_{\rm warm} = 2r_{\rm hot}$.

While the data do not favour all the outer disc being covered by the warm corona, they are (mostly) consistent with the idea that the disc underneath the warm Comptonizing material is passive, i.e. the optically thick material underneath the corona only reprocesses the luminosity dissipated further up in the disc (Petrucci et al. 2018). There is a trend seen also in Petrucci et al. (2018), $\Gamma_{\rm warm}$ is somewhat steeper for high $\dot{m}$, (e.g. PG1115+407 indicates some intrinsic power in the disc), and somewhat flatter at low $\dot{m}$ (e.g. NGC 5548). Steeper spectra can easily be produced with some intrinsic emission on the disc mid-plane. However, the lower spectral indices at low $\dot{m}$ are more difficult to explain.

Table 3. Parameters used in Sections 5.1 and 5.2.

System parameter	$r_{\rm out}$	$r_{\rm sg}$
	Inclination angle	45°
Hot inner flow	$T_{\rm e,hot}$	100 keV
	$\Gamma_{\rm hot}$	Calculated via equation (6)
	$L_{\rm diss,\,hot}$	$0.02L_{\rm Edd}$
Warm Compton	$T_{\rm warm}$	0.2 keV
	$\Gamma_{\rm e,warm}$	2.5
	$r_{\rm warm}$	$2r_{\rm hot}^{\dagger}$, $r_{\rm out}^{\ddagger}$
Reprocess		Included

Notes †Geometry of hot inner flow + warm Comptonizing skin + outer disc. ‡Geometry of hot inner flow + warm Comptonizing skin (i.e. without outer disc).

Petrucci et al. (2018) suggest that $\Gamma_{\rm warm} \leq 2.5$ is from partial covering of the corona over the passive mid-plane, so that some of the reprocessed photons do not re-intercept the warm Comptonization region to cool it. While this does indeed allow reprocessed photons to escape, this also means that these seed photons from the disc are seen directly which is not consistent with their assumption that the optical/UV is dominated by warm Comptonization alone, with no thermal emission from a disc (see also the discussion of this in Petrucci et al. 2018). Partial covering also seems physically unlikely as the optically thick, warm material has thermal pressure and so should expand outwards; so this additionally requires magnetic confinement. Instead, we suggest that the harder spectral indices could instead be produced by irradiation heating being more important at low $\dot{m}$ (see also Lawrence 2012). By definition, irradiation heats the photosphere at $\tau = 1$ rather than the deeper regions at $\tau =$ 10–20 where the majority of the warm Comptonization must be produced. We suggest that a more accurate treatment of an irradiated warm Comptonization region above a passive disc could produce the harder indices observed at low $\dot{m}$.

5 PREDICTIONS OF THE FULL SED MODEL FOR THE OBSERVATIONAL RESULTS

5.1 UV/X relation

We use the individual AGN fits to define the full SED model in order to compare to a large sample of objects spanning a wide range in $\dot{m} - M$. Lusso & Risaliti (2017) show that there is a well-defined relationship between the UV and X-ray luminosity of AGN, and claim this has low enough scatter to be used as a tracer of the cosmological expansion. Finding the underlying physics is then extremely important, as it can only be used with confidence when it is robustly understood.

Guided by the individual AGN fits above, we fix $L_{\rm diss,hot} = 0.02\,L_{\rm Edd}$, which defines $r_{\rm hot}$. We assume that the hot inner flow is quasi-spherical, and that the optically thick flow truncates at $r_{\rm hot}$ so that the spectral index, $\Gamma_{\rm hot}$, can be calculated from the ratio of dissipation in the hot region to intercepted seed photons. The best-fitting models above strongly support a geometry where there are three components, but again we compare the data to a model where the entire outer disc is covered by the warm Comptonizing material. The inclination angle is expected to be between 0° and 60° for type 1 AGN so we fix this at 45°. Full model parameters are shown in Table 3. The model with $r_{\rm warm} = 2r_{\rm hot}$ defines our simplified model QSOSED.

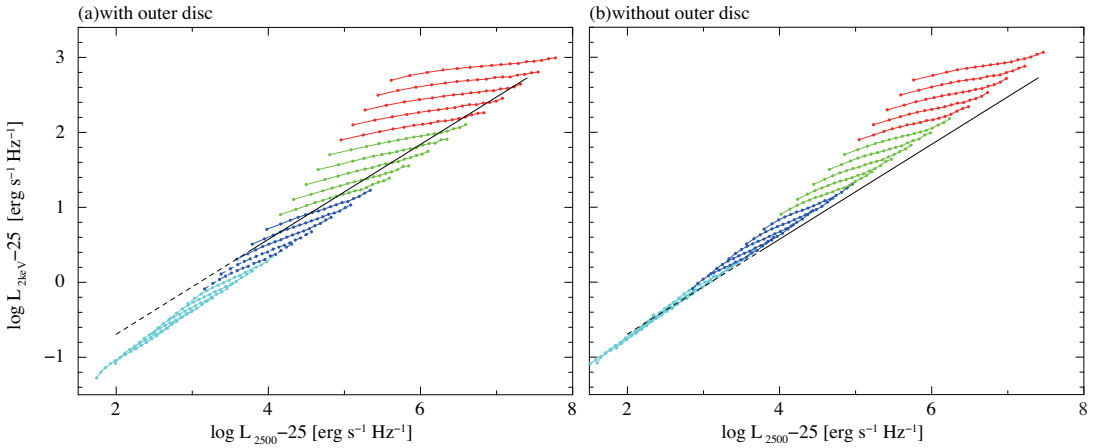

Figure 7. Monochromatic luminosities $\log L_X$ against $\log L_{UV}$. For black hole of $M = (0.1–1) \times 10^7\,M_\odot$ (cyan), $(0.16–1) \times 10^8\,M_\odot$ (blue), $(0.16–1) \times 10^9\,M_\odot$ (green), $(0.16–1) \times 10^{10}\,M_\odot$ (red). From left to right, $\dot{m}$ changes from 0.03 to 1. The observed UV/X relation in the range of $\log L_{2500} - 25 = 3.8–7.4$(fig. 3; Lusso & Risaliti 2017) is shown with a solid line. A dashed line is an extrapolation of the solid line. (a) Our three-component flow, with an outer disc, warm Comptonization region and hot inner flow. (b) A model where there is no standard outer disc.

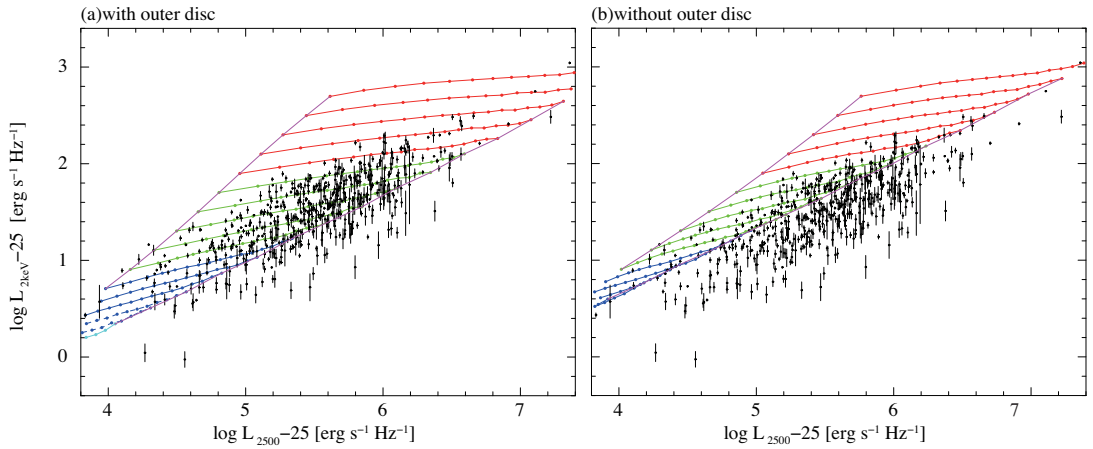

Figure 8. Enlargements of Fig. 7 are overlaid on the observed data points in fig. 3 of Lusso & Risaliti (2017) shown with open grey circles.

We calculate a grid of models spanning $\dot{m} = 0.03–1$ and $M = 10^6–10^{10}\,M_\odot$. This is consistent with the range of $\dot{m}$ and M in Lusso & Risaliti (2017) [The majority of their sample have $\dot{m} = 0.03–1$ and $(1–10)\times10^8\,M_\odot$; Lusso et al. 2012]. Fig. 7(a) shows the resulting relation between the monochromatic rest-frame luminosity at 2500 Å (i.e. 5 eV) and 2 keV, with lines connecting varying $\dot{m}$ for constant M from our model with an outer standard disc. Fig. 7(b) shows the slightly different predictions from a model where the warm Comptonization region covers the entire outer disc. Both these give a fairly well-defined correlation between the UV and X-rays, though with some scatter. We compare these to the best-fitting UV/X relation derived from 545 SDSS quasars by Lusso & Risaliti (2017) of

$$\log L_{2\,\mathrm{keV}} - 25 = 0.633 \cdot (\log L_{2500\,\text{Å}} - 25) - 1.959 \qquad (7)$$

(solid black line) in Figs 7(a) and (b). It is clear that the observed correlation is a slightly different slope than predicted by our models over this entire range. Our models with an outer disc match quite well to the observed relation at high masses (Fig. 7a), while models with just a warm Comptonization region are offset by their smaller predicted UV luminosity and match better at low masses (Fig. 7b).

Our predicted correlation is easy to understand, as it arises due to our assumptions that the X-ray flux is fixed at $L_X = 0.02\,L_{Edd} \propto M$ while the UV is from a disc/Comptonized disc so $L_{UV} \propto (M\dot{M})^{2/3} \propto (M^2\dot{m})^{2/3}$. Thus this predicts $\log L_X = \frac{3}{4}\log L_{UV} - \frac{1}{2}\log \dot{m} + b$ where b is a constant. There is clearly scatter in the models from $\dot{m}$, but the range should be constrained between 0.02 and 1. The lower limit is where the entire accretion flow is expected to make a transition to an ADAF (Narayan & Yi 1995), so that there is no bright UV emitting disc left; so there is no source of ionizing flux to excite a BLR. The upper limit comes from the expectation that super-Eddington objects are rare. Thus, there is only a limited range of 1.5 dex in $\dot{m}$, and this reduces to 0.75 dex with the square root factor. However, the data from Lusso & Risaliti (2017) have a scatter of only 0.2 dex.

We study the predicted behaviour in more detail in Fig. 8, using the individual data points from Lusso & Risaliti (2017) and Lusso (private communication). These are selected from the SDSS quasar sample, and so have absolute i-band magnitude brighter than −22. This already limits the black hole mass to $> 10^{7.5}\,M_\odot$ for objects with a standard disc below Eddington, and the masses reported in Lusso et al. (2012, their fig. 6) are clustered around $(1–10) \times 10^8\,M_\odot$. Thus, their data only include high black hole

masses, so our models with an outer standard disc match fairly well in normalization and slope to that observed (Fig. 8a), whereas models with complete coverage of the outer disc with a warm Comptonization underpredict the UV luminosity (Fig. 8b).

None the less, there is still a mismatch between the range predicted by our models and the observed data, even including an outer standard disc. The data extend to slightly higher UV luminosity than expected for Eddington-limited systems. Some of this can be inclination, as more face on systems will have stronger UV flux, but this makes only a difference of 0.15 dex between our assumed mean inclination of 45° and 0°. While this may explain the AGN not covered by the grid in the model with an outer standard disc, it is not enough to explain the larger number missed by the grid if the warm corona covers the entire outer disc. Instead, these require a substantial population of super-Eddington AGN. Super-Eddington AGN are seen in the local Universe (Jin, Done & Ward 2016; Done & Jin 2016; Jin et al. 2017), though they are rare, but their high UV luminosity enhances their probability of selection. We will extend the model to super-Eddington flows in a later work (Kubota & Done, in preparation), but note here that there are multiple uncertainties with the structure of these flows that make robust prediction difficult.

There is the opposite problem for the highest mass black holes at the lowest $\dot{m}$, where the grid extends into a region where there are no data points. We suggest that this could be due to selection effects. High-mass black holes are rarer, so require sampling a larger space volume in order to have a realistic probability of finding some. This means that they are generally seen at larger distances, so are only selected in flux-limited samples if they have high luminosity, weighting the selection of high-mass black holes towards higher $\dot{m}$ (including super-Eddington rates).

Thus, the observed UV/X-ray relation is predicted by our model, where the X-ray f is fixed at 0.02 $L_{\rm Edd}$ and the UV is from an outer standard disc, with selection effects (mostly the limited range of black hole mass) suppressing some of the predicted scatter. This is a very different explanation to that of Lusso & Risaliti (2017). Their 'toy' model uses the same standard disc equations to estimate the UV flux, but they set the X-ray flux using the gravitational power emitted from the outer disc down to the radius at which the disc becomes radiation pressure dominated. As they note in their paper, producing the X-rays at large radii in the disc rather than close to the black hole is in conflict with microlensing size scales, as well as with the rapid X-ray variability. We suggest that their model works because it effectively hardwires $L_{\rm X}$ to a constant value. The radius at which radiation pressure dominates in the disc, $R_{\rm rad}$, increases as $\dot{m}$ increases, so leaving a smaller and smaller fraction of power dissipated in the outer disc, and hence reproducing the observed decrease of $L_{\rm X}/L_{\rm bol}$ with $\dot{m}$ (Vasudevan & Fabian 2007).

Formally, this gives $R_{\rm rad} \propto (\alpha M)^{2/21} \dot{m}^{16/21} (1-f)^{6/7} R_{\rm g}$, where f is the fraction of the accretion power that is dissipated in the hard X-ray corona (Svensson & Zdziarski 1994). Then, the X-ray luminosity down through the corona from $R_{\rm out} - R_{\rm rad}$ is

$$L_{\rm X} \propto f G M \dot{M} / R_{\rm rad} \propto \alpha^{-2/21} M^{19/21} \dot{m}^{5/21} f (1-f)^{-6/7}$$

(see their equation 14 in detail). Hence $L_{\rm X}$ is roughly proportional to M and has only a weak dependence on $\dot{m}$, so their toy model is almost identical with our assumption of constant $L_{\rm diss,hot} = 0.02\, L_{\rm Edd}$.

Our model hardwires the same absolute value of $L_{\rm X}$, but in a much more plausible geometry where the X-ray source is produced close to the black hole, and with more physical motivation.

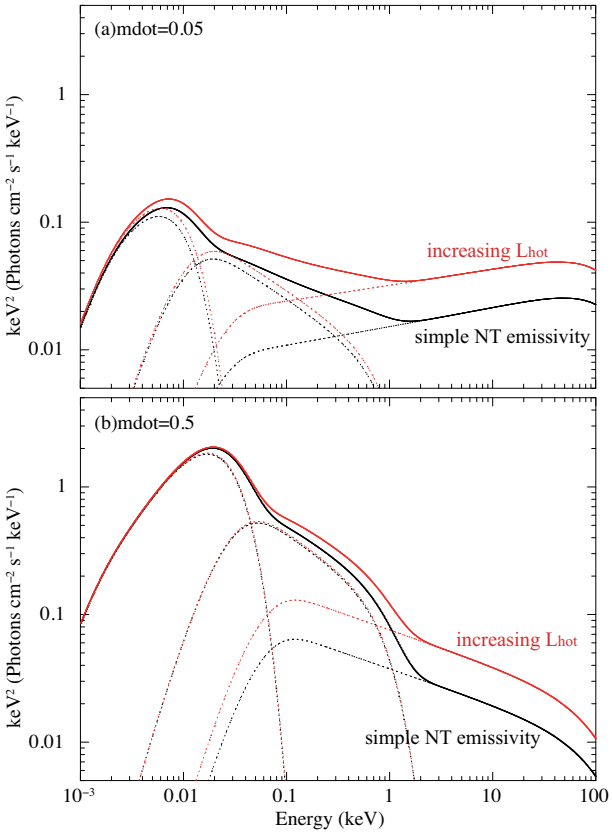

Figure 9. Effects of hard X-ray reprocess for a black hole of $M = 10^8\,{\rm M}_\odot$ with $\dot{m} = 0.05$ (a) and 0.5 (b). SEDs in which the hard X-ray luminosity is increased by a factor of 2.0 (red) are compared with those with NT emissivity with hard X-ray reprocess (black).

5.2 Optical variability

The X-rays vary rapidly in a stochastic manner about a mean, so their reprocessed emission should also carry the imprint of this rapid variability. The assumption in our SED is that the hard X-rays carry a fixed luminosity but arise from a smaller region as $\dot{m}$ increases. Hence, the reprocessed luminosity depends on $L_{\rm diss,\,hot} \times r_{\rm hot}$ (see Section 2.3) which decreases as $\dot{m}$ increases. This reprocessed flux is seen against the remaining, constant component from the disc, and/or warm Comptonization region which increases with $\dot{m}$. Thus, the variable reprocessed emission forms a smaller fraction of the optical/UV emission at higher $\dot{m}$, which qualitatively matches to what is observed (MacLeod et al. 2010; Ai et al. 2013; Kozlowski 2016; Simm et al. 2016).

Our model explicitly includes the reprocessed emission from X-ray illumination of the outer disc and warm Comptonization region, so here we calculate the contribution that the varying X-ray emission can make to the optical variability. We illustrate this with our three-component SED model, AGNSED (with all parameters as above, tabulated in Table 3 with $r_{\rm warm} = 2r_{\rm hot}$), for AGN of $10^8\,{\rm M}_\odot$ with $\dot{m} = 0.05$ and 0.5 in Figs 9(a) and (b), respectively. The black lines show spectra based on the simple NT emissivity including reprocessing, while red lines are the result of stochastic variability (so no impact on $\dot{m}$, $r_{\rm hot}$ etc.) increasing $L_{\rm hot}$ by a factor of 2. The emission from both the outer disc and warm Comptonizing region increases with the increase in $L_{\rm hot}$, and it is clear that reprocessing makes a much larger fraction of the optical emission at low accretion rates than at high ones.

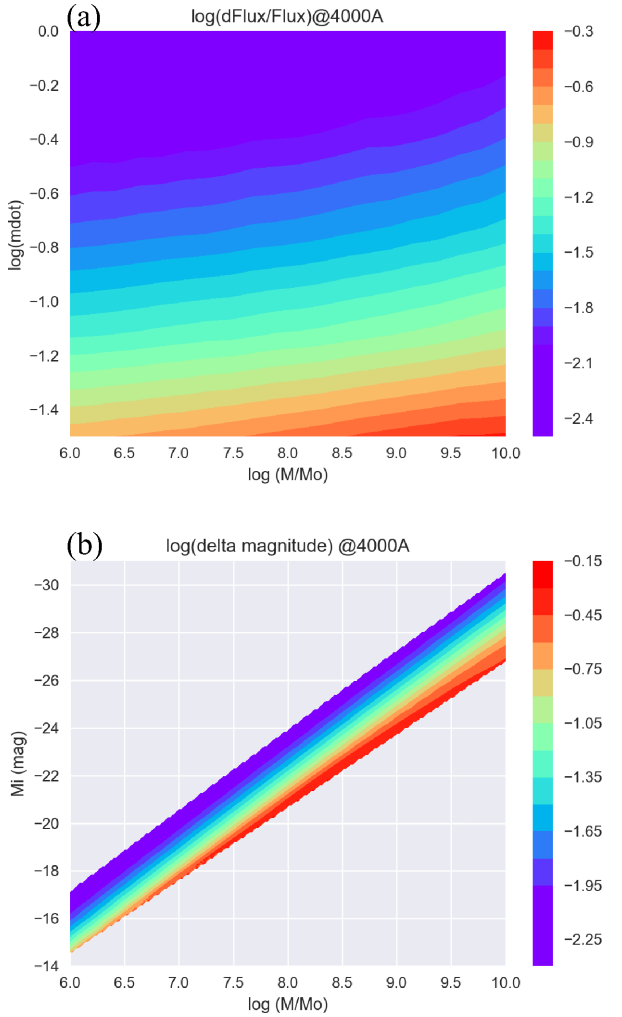

Figure 10. (a)The time variability $\log \Delta f_{4000}/f_{4000}$ are shown as colour grid of black hole mass $\log M/\mathrm{M}_{\odot}$ and $\log \dot{m}$. Hot X-ray emission is increased by a factor of 2.0. (b) Same as the top panel but $\log \Delta flux/flux$ and $\log \dot{m}$ are converted into $\log \Delta mag$ at 4000 Å and *i*-band absolute magnitude M_i. SEDs are based on the parameters of model (1) in Table 3.

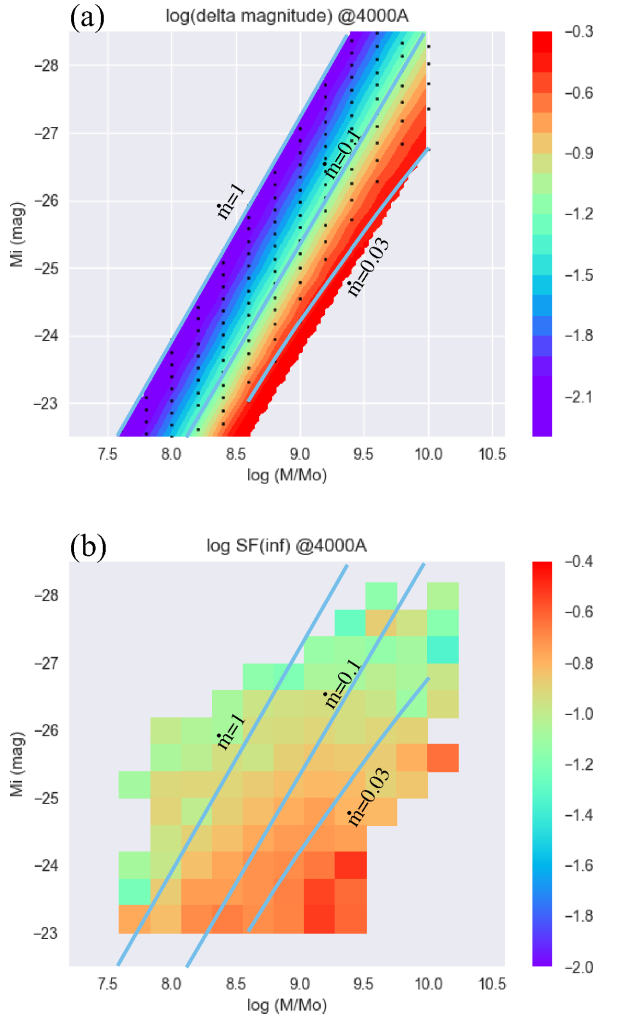

Figure 11. (a) Enlargement of Fig. 10(b). Black dots represent the places that we calculate. (b) $\log SF(\infty)$ at 4000 Å are plotted in space of M_i and $\log M/\mathrm{M}_{\odot}$(fig.14 in MacLeod et al. 2010). These data points are given by Macleod in private. Colour grid is the same between these two panels. Contours of constant Δmag in the top panel are overlaid on the bottom panel. Solid cyan lines show constant $\dot{m}$ of 0.03, 0.1, and 1.

We quantify the fractional change in optical flux at 4000 Å (3.1 eV), $\Delta f_{4000}/f_{4000}$, to a factor of 2 increase in $L_{\mathrm{diss,\,hot}}$ across the entire range of AGN masses ($M = 10^6 \sim 10^{10}\,\mathrm{M}_{\odot}$) and mass accretion rates ($\dot{m} = 0.03$–1). Fig. 10(a) shows this fractional variability as the colour coding across the grid of $\log M/\mathrm{M}_{\odot}$ and $\log \dot{m}$. It is obvious that lower $\dot{m}$ gives larger variability, though there is also a much smaller effect where the variability increases with larger mass. This occurs when reprocessing starts to affect the variability at the peak of the warm Comptonization region, where the temperature shift increases the amplitude of variability (see Fig. 3).

We match this to the observed amplitude of variability seen in a large sample of quasars in SDSS stripe 82. MacLeod et al. (2010) characterized the variability at rest frame 4000 Å with a damped random walk. The mean asymptotic amplitude of variability in optical magnitudes is characterized by the structure function extrapolated to infinite time, $SF(\infty)$. This is plotted as a function of *i*-band magnitude, M_i, and black hole mass in their fig. 14. In order to compare our models directly to their results, we convert our mass and $\dot{m}$ to M_i, and convert our fractional variability at 4000 Å to a magnitude difference ($2.5\Delta \log f_{4000} = \Delta m$). Fig. 10(b) shows this magnitude difference as a function of black hole mass and M_i across the whole range of models calculated in Fig. 10(a).

Fig. 11(a) shows a zoom of Fig. 10(b), limiting it to the same range in mass and M_i as used by MacLeod et al. (2010). This can then be compared directly against the data in Fig. 11(b) (Macleod, private communication). The range in M_i for each black hole mass spanned by our models at a given $\dot{m}$ is shown by the cyan lines for $\dot{m}$ of 0.03, 0.1, and 1. This makes it plan that the most variable AGN are those with implied $\dot{m} < 0.03$. These plausibly connect to the 'changing look' quasars if these are triggered by a state change from an outer disc to an ADAF flow (e.g. Noda & Done 2018).

Fig. 11(a) also stresses the need to use the non-linear conversion between optical flux and bolometric luminosity that is inherent in the standard disc equations. Hence, our data with $\dot{m} = 0.03$–1 do not span the entire range of M_i that are associated with this range in $\dot{m}$ in fig. 15 of MacLeod et al. (2010). There are again some AGN with $\dot{m} > 1$. These are rare (fig. 12 in MacLeod et al. 2010), but they considerably extend the range in M_i for the lowest mass AGN included here.

The colour grid is the same between Figs 11(a) and (b), and the models with a factor of 2 variability in X-rays give the observed amount of optical variability at $\dot{m} = 0.03$. Our models predict a weak trend for higher variability at higher black hole masses at fixed $\dot{m}$, which is opposite to the observed weak trend for higher variability at lower M but this may not be a serious discrepancy as the time-scales for the higher mass black holes are longer, which lead to some variability being missed. A much bigger discrepancy is that the models predict almost no variability at $\dot{m} = 1$, unlike the data that still show variability at the 10 per cent level. This clearly shows that some other component is required to make at least part of the optical variability, though the most rapid variability (e.g. from Kepler light curves; Aranzana et al. 2018) must arise from X-ray reprocessing. An additional source of longer term optical variability also matches with results from more intensive monitoring campaigns which stress the lack of correlation between the X-ray and optical light curves (e.g. Arévalo et al. 2009). Gardner & Done (2017) suggest that variability of the soft X-ray excess may play a role, but in our models here this still makes little impact on the optical spectrum at $\dot{m} = 1$. Instead, there should be intrinsic variability in the disc spectrum assuming our disc-dominated SED are the correct description of AGN close to the Eddington limit. Standard disc models do indeed predict that AGN discs should be highly unstable due to their dominant radiation pressure, but the non-linear outcome of what should be limit cycle variability is not yet known (Hameury et al. 2009 use a heating prescription that goes with only gas pressure to avoid complete disc disruption).

6 SUMMARY AND CONCLUSIONS

We construct a new spectral model AGNSED that includes an outer standard disc, a middle region where the disc is covered by optically thick, warm Comptonizing electrons, and an inner region of hot plasma that emits the power-law X-ray component. We assume that these regions are separated in radius, and that their emission is determined by the overall NT emissivity. This sets the size scale of the hot X-ray plasma and we include reprocessing of the X-rays from this source which illuminate the outer and warm Comptonizing disc.

We fit this model to multiwavelength SEDs of three well-observed AGN with very different Eddington ratios, NGC 5548 ($\dot{m} \sim 0.03$), Mrk 509 ($\dot{m} \sim 0.1$), and PG 1115 + 407 ($\dot{m} \sim 0.4$). The observed spectra are well reproduced with the model, and require an outer standard disc as well as a warm Comptonization component. This is different to conclusions from previous spectral fits as we constrain our warm Comptonization component to have seed photons and luminosity from an underlying disc rather than allowing these to be free parameters. The mid-plane disc is generally passive, i.e. the seed photons are produced by reprocessing rather than intrinsic dissipation, which sets the spectral index to $\Gamma_{\rm warm} = 2.5$ (Petrucci et al. 2018). The transition between the standard disc and warm Comptonization is always at temperatures consistent with the peak in UV opacity that might point to its origin in the changing disc structure due to failed UV line-driven winds (Laor & Davis 2014). The hot plasma has almost constant dissipation, consistent with 0.02–0.04 $L_{\rm Edd}$ for all $\dot{m}$. This implies a smaller size scale with increasing $\dot{m}$, as inferred from X-ray variability (McHardy et al. 2006). The hard X-ray spectral index is consistent with this dissipation always taking place in a region with no underlying disc, i.e. a truncated disc/hot inner flow geometry.

Fixing this derived geometry gives a full SED model that depends only on mass and mass accretion rate. This model successfully explains the observed tight UV/X relation shown by Lusso & Risaliti (2017) as a combination of the constant hard X-ray dissipation together with selection effects which mean that the rarer, higher mass quasars are seen preferentially at larger distances and so require higher Eddington fractions to be detected. This selection effect introduces scatter and bias but our model gives a physically based understanding of these factors, so that the relation can be used to probe cosmology.

The model includes the contribution to the optical/UV flux from X-ray illumination of the outer disc and warm Comptonization region. We calculate the optical variability resulting from a stochastic change in X-ray flux. This predicts the fast variability in optical should be a strongly decreasing function of Eddington fraction, as the fixed (average) hard X-ray dissipation is a smaller fraction of the bolometric luminosity at higher Eddington ratios. This matches to some of the trends seen in systematic surveys of AGN variability e.g. SDSS Stripe 82 (MacLeod et al. 2010), but there is more variability seen in high Eddington fraction AGN than predicted. This probably indicates that such highly radiation pressure dominated discs are somewhat unstable. This should motivate theoretical studies to give better understanding of such discs.

ACKNOWLEDGEMENTS

We thank M. Mehdipour for providing us SEDs in Mehdipour et al. (2011, 2015) and helpful comments on the data. We are also grateful to C. Macleod and E. Lusso for providing us the data points in MacLeod et al. (2010) and Lusso & Risaliti (2017), and useful discussions and comments. Special thanks to H. Noda and C. Jin for helpful discussions. AK is supported by research programme in foreign country by Shibaura Institute of Technology. CD acknowledges support from STFC (ST/P000541/1), and useful conversations with O. Blaes and J.M. Hameury. We also thank P.O. Petrucci as our referee for valuable comments.

REFERENCES

Ai Y. L., Yuan W., Zhou H., Wang T. G., Dong X.-B., Wang J. G., Lu H. L., 2013, AJ, 145, 90
Anders E., Ebihara M., 1982, Geochim. Cosmochim. Acta, 46, 2363
Aranzana E., Körding E., Uttley P., Scaringi S., Bloemen S., 2018, MNRAS, 476, 2501
Arévalo P., Uttley P., Lira P., Breedt E., McHardy I. M., Churazov E., 2009, MNRAS, 397, 2004
Beloborodov A. M., 1999, in Poutanen J., Svensson R., eds, ASP Conf. Ser. Vol. 161, High Energy Processes in Accreting Black Holes. Astron. Soc. Pac., San Francisco, p. 295
Boissay R., Ricci C., Paltani S., 2016, A&A, 588, A70
Brenneman L. W., Elvis M., Krongold Y., Liu Y., Mathur S., 2012, ApJ, 744, 13
Cappi M. et al., 2016, A&A, 592, A27
Crummy J., Fabian A. C., Gallo L., Ross R. R., 2006, MNRAS, 365, 1067
Czerny B., Nikołajuk M., Różańska A., Dumont A.-M., Loska Z., Zycki P. T., 2003, A&A, 412, 317
Davis S. W., Blaes O. M., Hubeny I., Turner N. J., 2005, ApJ, 621, 372
Davis S. W., Hubeny I., 2006, ApJS, 164, 530
Davis S. W., Woo J.-H., Blaes O. M., 2007, ApJ, 668, 682
De Marco B., Ponti G., Cappi M., Dadina M., Uttley P., Cackett E. M., Fabian A. C., Miniutti G., 2013, MNRAS, 431, 2441
Detmers R. G. et al., 2011, A&A, 534, A38
Dickey J. M., Lockman F. J., 1990, ARA&A, 28, 215
Done C., Jin C., 2016, MNRAS, 460, 1716
Done C., Davis S. W., Jin C., Blaes O., Ward M., 2012, MNRAS, 420, 1848 (D12)

Elvis M. et al., 1994, ApJS, 95, 1
Ezhikode S. H., Gandhi P., Done C., Ward M., Dewangan G. C., Misra R., Philip N. S., 2017, MNRAS, 472, 3492
Fabian A. C. et al., 2013, MNRAS, 429, 2917
Fabian A. C., Lohfink A., Kara E., Parker M. L., Vasudevan R., Reynolds C. S., 2015, MNRAS, 451, 4375
Gardner E., Done C., 2017, MNRAS, 470, 3591
Gierliński M., Done C., 2004a, MNRAS, 347, 885
Gierliński M., Done C., 2004b, MNRAS, 349, L7
Haardt F., Maraschi L., 1991, ApJ, 380, L51
Haardt F., Maraschi L., 1993, ApJ, 413, 507
Hameury J.-M., Viallet M., Lasota J.-P., 2009, A&A, 496, 413
Hubeny I., Blaes O., Krolik J. H., Agol E., 2001, ApJ, 559, 680
Jin C., Done C., Ward M., Gierliński M., Mullaney J., 2009, MNRAS, 398, L16
Jin C., Done C., Middleton M., Ward M., 2013, MNRAS, 436, 3173
Jin C., Done C., Ward M., 2016, MNRAS, 455. 691
Jin C., Done C., Ward M., Gardner E., 2017, MNRAS, 471, 706
Jin C., Ward M., Done C., Gelbord J., 2012a, MNRAS, 420, 1825
Jin C., Ward M., Done C., 2012b, MNRAS, 422, 3268
Kaastra J. S. et al., 2011a, A&A, 534, A36
Kaastra J. S. et al., 2011b, A&A, 534, A37
Kaastra J. S. et al., 2014, Science, 345, 64
Kalberla P. M. W., Burton W. B., Hartmann D., Arnal E. M., Bajaja E., Morras R., Pöppel W. G. L., 2005, A&A, 440, 775
Kozłowski S., 2016, ApJ, 826, 118
Kubota A., Makishima K., Ebisawa K., 2001, ApJ, 560, L147
Laor A., Davis S. W., 2011, MNRAS, 417, 681
Laor A., Davis S. W., 2014, MNRAS, 438, 3024
Laor A., Netzer H., 1989, MNRAS, 238, 897
Laor A., Fiore F., Elvis M., Wilkes B. J., McDowell J. C., 1997, ApJ, 477, 93
Lawrence A., 2012, MNRAS, 423, 451
Lubiński P. et al., 2016, MNRAS, 458, 2454
Lusso E. et al., 2012, MNRAS, 425, 623
Lusso E., Risaliti G., 2017, A&A, 602, A79
McHardy I. M., Koerding E., Knigge C., Uttley P., Fender R. P., 2006, Nature, 444, 730
MacLeod C. L. et al., 2010, ApJ, 721, 1014
Magdziarz P., Zdziarski A. A., 1995, MNRAS, 273, 837
Magdziarz P., Blaes O. M., Zdziarski A. A., Johnson W. N., Smith D. A., 1998, MNRAS, 301, 179
Malzac J., Dumont A. M., Mouchet M., 2005, A&A, 430, 761
Matt G. et al., 2014, MNRAS, 439, 3016
Matzeu G. A., Reeves J. N., Nardini E., Braito V., Turner T. J., Costa M. T., 2017, MNRAS, 465, 2804
Mehdipour M. et al., 2011, A&A, 534, A39
Mehdipour M. et al., 2015, A&A, 575, A22
Middei R., et al., 2018, A&A, preprint (arXiv:1803.07334)
Mitsuda K. et al., 1984, PASJ, 36, 741
Nandra K., O'Neill P. M., George I. M., Reeves J. N., 2007, MNRAS, 382, 194
Narayan R., Yi I., 1995, ApJ, 452, 710
Noda H., Done C., 2018, MNRAS, preprint (arXiv:1805.07873)
Noda H., Makishima K., Nakazawa K., Uchiyama H., Yamada S., Sakurai S., 2013, PASJ, 65, 4
Novikov I. D., Thorne K. S., 1973, in DeWitt C., DeWitt B., eds, Black holes. Gordon and Breach, N.Y., p. 343
Petrucci P.-O. et al., 2013, A&A, 549, A73
Petrucci P. O., Ursini F., De Rosa A., Bianchi S., Cappi M., Matt G., Dadina M., Malzac J., 2018, A&A, 611, A59
Porquet D., Reeves J. N., O'Brien P., Brinkmann W., 2004, A&A, 422, 85
Porquet D. et al., 2018, A&A, 609, A42
Poutanen J., Veledina A., Zdziarski A. A., 2018, A&A, 614, A79
Proga D., Stone J. M., Kallman T. R., 2000, ApJ, 543, 686
Richards G. T. et al., 2006, ApJS, 166, 470
Różańska A., Malzac J., Belmont R., Czerny B., Petrucci P.-O., 2015, A&A, 580, A77
Shakura N. I., Sunyaev R. A., 1973, A&A, 24, 337
Shemmer O., Brandt W. N., Netzer H., Maiolino R., Kaspi S., 2006, ApJ, 646, L29
Shemmer O., Brandt W. N., Netzer H., Maiolino R., Kaspi S., 2008, ApJ, 682, 81
Simm T., Salvato M., Saglia R., Ponti G., Lanzuisi G., Trakhtenbrot B., Nandra K., Bender R., 2016, A&A, 585, A129
Singh K. P., Garmire G. P., Nousek J., 1985, ApJ, 297, 633
Steiner J. F., Narayan R., McClintock J. E., Ebisawa K., 2009, PASP, 121, 1279
Stern B. E., Poutanen J., Svensson R., Sikora M., Begelman M. C., 1995, ApJ, 449, L13
Svensson R., Zdziarski A. A., 1994, ApJ, 436, 599
Ursini F. et al., 2015, A&A, 577, A38
Vasudevan R. V., Fabian A. C., 2007, MNRAS, 381, 1235
Vasudevan R. V., Fabian A. C., 2009, MNRAS, 392, 1124
Wright E. L., 2006, PASP, 118, 1711
Yaqoob T., George I. M., Nandra K., Turner T. J., Serlemitsos P. J., Mushotzky R. F., 2001, ApJ, 546, 759
Yaqoob T., Turner T. J., Tatum M. M., Trevor M., Scholtes A., 2016, MNRAS, 462, 4038
Zdziarski A. A., Johnson W. N., Magdziarz P., 1996, MNRAS, 283, 193
Zdziarski A. A., Lubiński P., Smith D. A., 1999, MNRAS, 303, L11
Zheng W., Kriss G. A., Telfer R. C., Grimes J. P., Davidsen A. F., 1997, ApJ, 475, 469
Życki P. T., Done C., Smith D. A., 1999, MNRAS, 309, 561

APPENDIX A: PARAMETERS OF THE MODEL

We show all the spectral parameters of AGNSED in Table A1. In the public version of AGNSED, albedo is fixed at $a = 0.3$. Seed photon temperature for the hot Comptonization component is calculated internally (see Section 2.2). $r_{\rm hot}$ is adopted as a fitting parameter instead of $L_{\rm diss,\,hot}$. The model has some switching parameters. If parameter 6 is negative, the model gives the hot Comptonization component. And if parameter 7 is negative, the model gives the warm Comptonization component. If parameter 9 is negative, the model gives the outer disc. If parameter 12 is negative, the code will use the self-gravity radius as calculated from Laor & Netzer (1989).

QSOSED is the simplified version of AGNSED by fixing some parameters at the typical values and by including reprocessing. The spectral parameters are shown in Table A2. The rest of the parameters are fixed at $kT_{\rm e,\,hot} = 100$ keV, $kT_{\rm e,\,warm} = 0.2$ keV, $\Gamma_{\rm warm} = 2.5$, $r_{\rm warm} = 2r_{\rm hot}$, $r_{\rm out} = r_{\rm sg}$, and $h_{\rm max} = 100$. Also, $\Gamma_{\rm hot}$ is calculated via equation (6) and $r_{\rm hot}$ is calculated to satisfy $L_{\rm diss,hot} = 0.02\,L_{\rm Edd}$.

Table A1. Parameters in AGNSED.

Par1	Mass, black hole mass in solar masses.
Par2	Dist, comoving (proper) distance in Mpc.
Par3	$\log \dot{m}$, $\dot{m} = \dot{M}/\dot{M}_{\rm Edd}$ where $\eta \dot{M}_{\rm Edd} c^2 = L_{\rm Edd}$.
Par4	$a*$, dimensionless black hole spin.
Par5	$\cos i$, inclination angle i for the warm Comptonizing component and the outer disc.
Par6	$kT_{\rm e,hot}$, electron temperature for the hot Comptonization component in keV. If this parameter is negative then only the hot Comptonization component is used.
Par7	$kT_{\rm e,warm}$, electron temperature for the warm Comptonization component in keV. If this parameter is negative then only the warm Comptonization component is used.
Par8	$\Gamma_{\rm hot}$, spectral index of the hot Comptonization component. If this parameter is negative, the code will use the value calculated via equation (6).
Par9	$\Gamma_{\rm warm}$, spectral index of the warm Comptonization component. If this parameter is negative then only the outer disc component is used.
Par10	$r_{\rm hot}$, outer radius of the hot Comptonization component in $R_{\rm g}$.
Par11	$r_{\rm warm}$, outer radius of the warm Comptonization component in $R_{\rm g}$.
Par12	$\log r_{\rm out}$, log of the outer radius of the disc in units of $R_{\rm g}$. If this parameter is negative, the code will use the self-gravity radius as calculated from Laor & Netzer (1989).
Par13	$h_{\rm max}$, the upper limit of the scaleheight for the hot Comptonization component in $R_{\rm g}$. If this parameter is smaller than parameter 10, the hot Comptonization region is a sphere of radius $h_{\rm max}$ by keeping $L_{\rm diss,\,hot}$ determined by $r_{\rm hot}$ via equation (2).
Par14	Switching parameter for the reprocessing, 0 or 1. If this parameter is 0, reprocessing is not considered. If this parameter is 1, reprocessing is included.
Par15	Redshift

Table A2. Parameters in QSOSED.

Par1	Mass, black hole mass in solar masses.
Par2	Dist, comoving (proper) distance in Mpc.
Par3	$\log \dot{m}$, $\dot{m} = \dot{M}/\dot{M}_{\rm Edd}$ where $\eta \dot{M}_{\rm Edd} c^2 = L_{\rm Edd}$.
Par4	$a*$, dimensionless black hole spin.
Par5	$\cos i$, inclination angle i for the warm Comptonizing component and the outer disc.
Par6	Redshift

This paper has been typeset from a TEX/LATEX file prepared by the author.